

# **APPLIED PHYSICS REVIEWS**

# Near-ultraviolet Raman and micro-Raman analysis of electronic materials

Mohammad Nazari<sup>1</sup> and Mark W. Holtz<sup>1,2,a)</sup>

<sup>1</sup>Materials Science, Engineering, and Commercialization, Texas State University, San Marcos, Texas 78666, USA

(Received 1 September 2018; accepted 30 October 2018; published online 26 November 2018)

Raman and micro-Raman analysis methods have been extensively investigated for the study of materials used in electronic and photonic devices. Raman studies are used to understand fundamental phonon properties, along with effects related to the crystal structure, disorder, doping, and external factors such as temperature and stress. Micro-Raman extends these investigations to the micron scale. This article reviews diverse benefits of Raman measurements when carried out using laser excitation in the near-ultraviolet wavelength range, nominally 400 to 325 nm. Micro-Raman methods in the near ultraviolet exploit the key advantage of reduced focal spot size, achievable at shorter wavelengths when using diffraction-limited optics, for mapping with high spatial resolution. There are distinct advantages common to Raman and micro-Raman spectroscopy in the near ultraviolet when compared to the widely used visible excitation. One advantage exploits the shallower optical penetration depth in select materials for probing near-surface regions or interfaces. A second advantage is related to tuning of the excitation photon energy relative to the electronic levels of a material for investigating resonance effects. Finally, the application of Raman scattering to materials which exhibit strong fluorescence requires tuning to a wavelength range away from the potentially obscuring emission. This article overviews several examples of these key advantages to study diverse applied physics problems in electronic and photonic materials. Topics covered include stress mapping in silicon and related materials, stress and thermal effects in gallium nitride and other group-III-nitride semiconductors, and carbon materials ranging from graphite and graphene to diamond grown using chemical vapor deposition. The fundamental effects of stress- and temperature-induced shifts in phonon energies and their application to study epitaxy and devicerelated effects are also briefly reviewed. Published by AIP Publishing. https://doi.org/10.1063/1.5054660

# **TABLE OF CONTENTS**

I. INTRODUCTION	1
II. BACKGROUND	2
III. UV MICRO-RAMAN METHODS	4
IV. STRESS AND COMPOSITION IN SILICON	
AND RELATED MATERIALS	6
V. STRESS AND THERMAL PROPERTIES OF	
GROUP-III-NITRIDE MATERIALS AND	
DEVICES	11
VI. CARBON	14
VII. SUMMARY	17

### I. INTRODUCTION

Raman spectroscopy has been extensively developed for investigating diverse materials in condensed matter physics.

Numerous reviews have been previously published emphasizing Raman scattering in semiconductors and other electronic materials. Investigations have been carried out for understanding fundamental properties of, and processes in, these materials and for the study of properties related to device applications. The majority of this work has been carried out using visible Raman spectroscopy due, in part, to the widespread availability of intense, narrow excitation lines from ion lasers and the routine availability of optical components in the visible wavelength ( $\lambda$ ) range. Far fewer studies have been conducted in the ultraviolet (UV). In this review, we describe key attributes and corresponding select applications of near-UV Raman and micro-Raman studies.

There are distinct advantages for probing materials via Raman spectroscopy in the UV. One such advantage is the exploitation of resonance-related effects obtained by varying the excitation photon energy ( $\hbar\omega$ ) to tune *into* a specific transition or across a range of transitions. This approach is useful in probing phenomena related to the electronic structure of materials and for achieving intensity enhancements through resonance. <sup>17–22</sup> In select cases, it is of interest to tune away

<sup>&</sup>lt;sup>2</sup>Department of Physics, Texas State University, San Marcos, Texas 78666, USA

a) Author to whom correspondence should be addressed: Mark.Holtz@ txstate.edu

from resonance conditions as in the case of NiO.<sup>23</sup> An affiliated advantage is the use of excitation wavelengths to tune *away* from intense fluorescence in various materials. In doing so, a measurement range may be established where the fluorescence intensity is relatively weak so that Raman spectra are obtainable.

Micro-Raman measurements are useful for probing a small sample volume. In this regard, UV light may be advantageous for producing a smaller lateral laser *focus diameter* than visible light, provided that diffraction-limited optics are attainable. In considering the need to design suitable optics, we encounter a strong division between near and deep UV ranges. In the near-UV range, optical components are available and even the same as what are used in visible micro-Raman studies. In the deep UV, however, optical materials are difficult to obtain, making these measurements challenging. Despite this limitation, deep-UV Raman studies have been previously reported. 9,24-26 Here, we restrict our attention to the near-UV wavelength range for both Raman and micro-Raman studies.

In addition to reduced laser spot size, when using near-UV light for micro-Raman spectroscopy, tuning to this range produces a fourth advantage for these studies. Probing materials that absorb light strongly in the UV results in a *shallower optical penetration depth*  $(d_{opt})$ . These measurements may then be applied to provide information about the near-surface (or interface) regime of a material. In this article, we review case studies exploiting each of these advantages in near-UV Raman and micro-Raman spectroscopy.

We organize this review as follows: In Sec. II, we briefly review basic concepts that are relevant to micro-Raman studies in electronic materials, including their application to the local measurement of temperature rise and stress. In Sec. III, we overview experimental factors specifically related to conducting Raman and micro-Raman measurements in the near UV. In Sec. IV, we examine the first applications of near-UV micro-Raman studies to stress mapping in silicon and Raman measurements in related materials. Section V discusses application to GaN and related group-III-nitride devices. Several Raman and micro-Raman investigations of carbon compounds, with emphasis on diamond, are described in Sec. VI. We briefly summarize in Sec. VII. A list of common symbols and acronyms is included in Table I.

### II. BACKGROUND

Raman spectroscopy has been used to investigate effects related to crystal quality, defects, disorder, structural phase, polytype, alloy composition, local stress, and temperature. Much of this work has focused on the technologically important semiconductors, and numerous overviews have been published. <sup>1–16</sup> Here, we include brief descriptions of what is most relevant in micro-Raman mapping.

First-order Raman scattering in crystalline materials is subject to energy and crystal-momentum conservation principles 27,28

$$\hbar\omega_S = \hbar\omega_L \pm \hbar\omega_p, \tag{1a}$$

$$\hbar \mathbf{k}_S = \hbar \mathbf{k}_L + \hbar \mathbf{k}_p \pm \hbar \mathbf{K}, \tag{1b}$$

where  $\hbar$  is Planck's constant and  $\hbar\omega$  is the energy of the laser (L) excitation photon, scattered (S) photon, or phonon (p) either created (-, Stokes) or annihilated (+, anti-Stokes) in the Raman process. For convenience, phonon energy is generally expressed in energy  $(1/\lambda)$  with units cm $^{-1}$ . The  $\hbar k$  momentum terms in Eq. (1b) are analogously labeled with the last term accounting for a reciprocal lattice vector (K). The nearly vertical dispersion of light, relative to the size of the first Brillouin zone, results in the important  $k_p \approx 0$  selection rule for first-order Raman scattering in crystals. The other selection rules are derived from the polarization of the incident and scattered light,  $e_{L(S)}$ , and the propagation and polarization properties of the phonons in a particular crystal symmetry according to

$$\frac{I_S}{I_{AS}} > \sim I_0 V \omega_L \omega_S^3 \sum_j |\boldsymbol{e}_L \cdot \boldsymbol{R}_j \cdot \boldsymbol{e}_S|^2 \begin{cases} n_B(\omega_p, T) + 1, \text{ Stokes} \\ n_B(\omega_p, T), \text{ anti } - \text{ Stokes}, \end{cases}$$
(2)

where  $I_0$  is the incident laser intensity, V is the scattering volume, and  $R_j$  is the Raman tensor for the phonon of the crystal structure being measured with j the displacement direction.  $I_S$  is the Stokes (S), and  $I_{AS}$  the anti-Stokes (AS) scattering intensity. The quantity  $n_B(\omega, T)$  is the Bose function at energy  $\hbar\omega$  and absolute temperature T.

The  $k_p \approx 0$  selection rule, permitting only zone-center optical phonons to participate in the first-order Raman process, results in the sharp spectral features needed for many of the investigations described here. Examples include the

TABLE I. List of common symbols and acronyms used in this article.

Quantity	Symbol	Term	Acronym	
emperature $T, \Delta T$		Ultraviolet	UV	
Pressure	P	Light-emitting diode	LED	
Volume	V	High electron mobility transistor	HEMT	
Stress	$\sigma$	Chemical vapor deposition	CVD	
Wavelength	λ	Coefficient of thermal expansion	CTE	
Frequency (photon or phonon)	$\omega$	Transmission electron microscopy	TEM	
Wavevector	k	Reciprocal space map	RSM	
Bose function	$n_B(\omega,T)$	High-resolution X-ray diffraction	HRXRD	
Optical absorption coefficient	α	Two-dimensional electron gas	2DEG	
Optical penetration depth	$d_{opt}$	Thermal boundary resistance	TBR	
Thermal conductivity	$\kappa$			

application of Raman spectroscopy to understand the effects of external and substrate-induced stresses and the effects of external temperature changes in crystalline materials. To illustrate the latter in the most straightforward case of isotropic volume deformation, the phonon temperature shift may be written as

$$\frac{d\omega}{dT} = \left(\frac{\partial\omega}{\partial T}\right)_V + \left(\frac{\partial V}{\partial T}\right) \left(\frac{\partial\omega}{\partial V}\right)_T,\tag{3}$$

where the explicit (first) term in Eq. (3) describes intrinsic effects of temperature on phonon energy. The implicit (second) term accounts for temperature-induced volume changes (thermal expansion) and the effects of volume deformation on phonon energies. The second term therefore includes strain- (stress-) induced shifts in phonon energies.

For the simplest stress case of hydrostatic deformation, Eq. (3) may be rewritten as

$$\frac{d\omega}{dT} = \left(\frac{\partial\omega}{\partial T}\right)_V + \beta_P V \left(\frac{\partial\omega}{\partial V}\right)_T,\tag{4}$$

where  $\beta_P = \frac{1}{V} \left( \frac{\partial V}{\partial T} \right)_P$  is the volume thermal expansion coefficient.<sup>29</sup> With the help of the scaling relation  $\omega/\omega_0 = (V_0/V)^{\gamma}$ , where  $\gamma$  is the Grüneisen parameter, the second term in Eq. (4) may be written as

$$-\gamma\omega_0\beta_P,$$
 (5)

where  $\omega$  has been replaced by the phonon energy at the reference condition  $\omega_0$  which is generally valid since shifts  $\Delta\omega\ll\omega_0$ . For the commonly encountered non-hydrostatic deformations, the strain tensor e must be considered along with its effect on phonon energies. The quantity more often studied in Raman and micro-Raman measurements is stress  $(\sigma)$ , which is related to strain by Hooke's law through the rank-four elastic compliance tensor S through  $\sigma=Se$ . Changes in strain due to variations in temperature are quantified by means of the linear coefficient of thermal expansion (CTE) defined as

$$\beta_i = \frac{1}{a_{i0}} \left( \frac{\partial a_i}{\partial T} \right)_P = \left( \frac{\partial e_i}{\partial T} \right)_P, \tag{6}$$

where  $e_i$  is the strain along the *i*th crystal axis having lattice constant  $a_i$ . Equation (6) also helps in phenomenologically linking the isotropic expression in Eq. (5) with more general strain situations, including the biaxial deformation common in epitaxy.

Internal residual or external applied stress may be estimated using Raman scattering. A simple approach for using the Raman (red or blue) shift, relative to a reference unstrained phonon position, can be utilized to estimate stress according to

$$\omega = \omega_0 + k_S \sigma_{xx},\tag{7}$$

where  $k_S$  is the so-called Raman stress factor. Here, the blue-shift (redshift) in the peak position corresponds to compressive (tensile) stress and therefore  $\sigma_{xx} < 0$  ( $\sigma_{xx} > 0$ ). This

approach can be applied to map the stress across large wafers. Raman stress factors are summarized for select materials in Table II, along with percent uncertainty in estimated stress using Eq. (7) with  $\Delta\omega = \omega - \omega_0 = 1 \, \mathrm{cm}^{-1}$  and assuming uncertainties in the measured values  $\delta\omega = \delta\omega_0 = 0.1 \, \mathrm{cm}^{-1}$ .

Local temperature, at the measurement position, can also be estimated from three Raman-based quantities. The first is by measuring the Stokes (S) to anti-Stokes (AS) intensity ratio,  $I_S/I_{AS}$ , and using Eq. (2). The temperature dependence is present in the Bose functions. For transparent media, the scattering volume in this ratio cancels. In opaque media, the depth attribute of the scattering volume is replaced by the wavelength-dependent optical penetration depth  $(d_{opt})$  discussed in more detail in Sec. III. For layers of thickness t on the order of  $d_{opt}$  or thinner, the scattering volume is replaced with  $d_{opt}(1-e^{-t/d_{opt}})$ . The direct measurement of  $I_S/I_{AS}$  now allows estimation of absolute sample temperature. Despite the elegance of this method, experimental factors including weak AS scattering and a wavelength-dependent instrument response, for measuring intensity, limit the applicability.

A second approach for estimating material temperature is to examine the phonon linewidth ( $\Gamma_{ph}$ ). For bulk crystals, having high purity, the phonon energy and linewidth depend on temperature through their finite lifetimes. Broadening may be interpreted based on factors that limit lifetime ( $\tau$ ) according to

$$2\pi c \Gamma_{ph} = \frac{1}{\tau} = \frac{1}{\tau_{intrinsic}} + \frac{1}{\tau_{extrinsic}}, \tag{8}$$

where c is the speed of light,  $\tau_{extrinsic}$  represents the lifetime due to (lumped) effects of phonon-impurity/defect scattering, and  $\tau_{intrinsic}$  is the intrinsic lifetime limited by phonon decay. The zone-center optical phonons may decay into multiple lower-energy vibrations, provided that energy and crystal momentum are conserved in any individual process. Generally, the lowest-order allowed processes (e.g., two child phonon) are fastest and dominate the linewidth. Two-

TABLE II. Raman stress coefficients,  $k_S$ , for different materials and relative uncertainty in stress estimated from Eq. (7).

Material	Phonon	$k_S  (\mathrm{cm}^{-1}/\mathrm{GPa})$	$\frac{\delta(\sigma_{xx})/\sigma_{xx} (\%)}{14}$	
Si	$O(\Gamma)$	$-1.88 \pm 0.05^{31}$		
c-BN	LO	$-3.45 \pm 0.07^{32}$		
	TO	$-3.39 \pm 0.08$		
Bulk diamond	$O(\Gamma)$	$-3.2 \pm 0.2^{33}$	16	
		(hydrostatic)		
CVD diamond	$O(\Gamma)$	$-0.53^{5}$		
GaN	$E_2^2$	$-3.4 \pm 0.3^{34}$	17	
	-	$-3.885 \pm 0.017^{35}$	14	
GaN	$A_1(LO)$	$-2.14 \pm 0.28^{34}$	19	
AlN	$E_2^2$	$-6.3 \pm 1.4^{36}$	26	
	$A_1(LO)$	$-4.88 \pm 0.08^{32}$	14	
		$-3.9 \pm 0.2$	15	
6H-SiC	LO	$3.56 \pm 0.02^{37}$	14	
	TO	$-2.92 \pm 0.01$		

phonon decay processes are classified as the so-called Klemens (symmetric)<sup>38</sup> and Ridley (asymmetric).<sup>39</sup> The related temperature dependence of the linewidth may be written as

$$\Gamma_{intrinsic}(T) \sim \begin{cases} (1 + 2n(\omega_0/2, T)), \text{ Klemens} \\ (1 + n(\omega_1, T) + n(\omega_2, T)), \text{ Ridley}, \end{cases}$$
 (9)

where  $\omega_0 = \omega_1 + \omega_2$  represents the parent (subscript 0) and child (1,2) phonon energies. As expected, the Ridley process reduces to Klemens when  $\omega_1 = \omega_2 = \omega_0/2$ . When  $k_BT > \hbar\omega$ , we may approximate  $n(\omega,T) \sim k_BT/\hbar\omega$  to obtain a linear dependence, providing a straightforward temperature dependence. When the two-phonon decay processes are forbidden by the conservation principles, higher-order processes are required to describe the phenomenon, lifetimes rise, and the thermal broadening slows. Generally, the linewidth is a weak function of temperature, making it less desirable for temperature evaluation.

The most straightforward approach for estimating temperature changes via Raman scattering is the shift in the phonon position. The intrinsic shift is due to phonon decay and related to the above expression for  $\Gamma_{intrinsic}(T)$  by a Kramers-Kronig transformation. Looking at the case of a uniaxial material, such as the group-III-nitride semiconductor GaN, the phonon shift may be written as

$$\Delta\omega = \omega(T) - \omega_0$$

$$= -\omega_0 \gamma \int_0^T \left[ \beta_c(T') + 2\beta_a(T') \right] dT'$$

$$- A(1 + n(\omega_1, T) + n(\omega_2, T)), \tag{10}$$

where the first term in the last expression on the right originates from the effects of thermal expansion. In general, it is important to properly treat the temperature dependence of the CTE. However, above cryogenic temperatures,  $\beta$  changes gradually so that the integral, along with the Bose functions  $(k_BT > \hbar\omega)$ , may be approximated as linear functions in T

$$\omega(T) = \omega_0 + k_T \Delta T, \tag{11}$$

with  $k_T$  being the phonon temperature coefficient. This expression is the basis for using Raman studies to measure temperature and is particularly useful for determining  $\Delta T$  relative to an ambient reference temperature.

The temperature coefficient  $k_T$  in Eq. (11) is determined empirically. Coefficients for a selection of materials are summarized in Table III. The relative temperature uncertainty,  $\frac{\delta(\Delta T)}{\Delta T}(\%)$ , using Eq. (11) is due to the uncertainty in fitting Raman peaks which manifests itself in measuring  $\omega$  and  $\omega_0$  and estimating  $k_T$  from the calibration measurements. The error in fitting the phonon peak position depends on Raman intensity. Typical uncertainties are from peak fitting ( $\delta\omega$ ) in the 0.10 to 0.01 cm<sup>-1</sup> range. Choosing an appropriate value of  $k_T$  depends on the temperature range of interest, as it is clear for GaN and AlN cases. Measurements between 200 K and 300 K give smaller (absolute) values of  $k_R$  compared to values obtained from a higher temperature range of

TABLE III. Raman temperature coefficient,  $k_T$ , for different materials. The temperature range corresponds to what was used by the referenced source in determining the coefficient.

Material	Phonon	Temperature range (K)	$k_T  (\mathrm{cm}^{-1}/\mathrm{K})$
Silicon (bulk)	$O(\Gamma)$	300–400 <sup>a</sup>	$-0.02501 \pm 0.0004$
Diamond (bulk)	$O(\Gamma)$		$-0.0112 \pm 0.0003$
Diamond (CVD)			$-0.0150 \pm 0.0003$
GaAs	TO	150-300 <sup>55</sup>	$-0.0175 \pm 0.0008$
	LO		$-0.0172 \pm 0.0012$
InP	TO		$-0.0161 \pm 0.0004$
	LO		$-0.0159 \pm 0.001$
Cubic GaN	TO	300–750 <sup>56</sup>	$-0.0157 \pm 0.0006$
	LO		$-0.0311 \pm 0.002$
GaN	$E_2^2$	200–300 <sup>57</sup>	$-0.0079 \pm 0.0005$
		300-800 <sup>58</sup>	$-0.0183 \pm 0.0007$
		300-800 <sup>59</sup>	$-0.0215 \pm 0.0013$
	$A_1(LO)$	200–300 <sup>57</sup>	$-0.0211 \pm 0.0002$
		$300-800^{58}$	$-0.0315 \pm 0.0009$
		300-800 <sup>59</sup>	$-0.0223 \pm 0.0097$
AlN	$E_2^2$	200–300 <sup>57</sup>	$-0.0164 \pm 0.001$
		300-800 <sup>58</sup>	$-0.0278 \pm 0.0008$
		300–1275 <sup>60</sup>	$-0.0222 \pm 0.0002$
	$A_1(LO)$	200–300 <sup>57</sup>	$-0.0229 \pm 0.0008$
		300-800 <sup>58</sup>	$-0.0395 \pm 0.0024$
		300–1275 <sup>60</sup>	$-0.0281 \pm 0.0006$
h-BN	$E_2^2$	300–400 <sup>a</sup>	$-0.0203 \pm 0.0003$

<sup>&</sup>lt;sup>a</sup>Not previously published.

300 to 800 K. This may be due, in part, to the validity of the high-temperature approximation when simplifying the Bose functions. The temperature uncertainty using Eq. (11) can be calculated by uncertainty propagation according

to 
$$\frac{\delta(\Delta T)}{\Delta T}(\%) = 100 \times \sqrt{\left(\frac{\delta(\Delta \omega)}{\Delta \omega}\right)^2 + \left(\frac{\delta k_T}{k_T}\right)^2}$$
, where  $\delta(\Delta \omega)$  =  $\sqrt{\left(\delta\omega\right)^2 + \left(\delta\omega_0\right)^2} \approx \sqrt{2}\delta\omega$ . Based on the reported uncertainties in  $k_T$ , the relative uncertainty  $\frac{\delta(\Delta T)}{\Delta T}(\%)$  in measuring temperature this way is high for materials at a small phonon

shift, as expected. Generally, a phonon shift of  $\sim 1.5 \,\mathrm{cm}^{-1}$  results in temperature estimates with uncertainties below 10%.

We close this section by providing guidance to several additional resources. Analytical approaches to calculating stresses from patterned layers, such as what is common in semiconductor manufacturing, have been reviewed by Hu. <sup>42</sup> Both stress and strain may also be simulated using finite element (FE) analysis. <sup>43–49</sup> The effects of strain and stress on phonon properties have been extensively studied. <sup>5,11,32–34,37,50,51</sup> The application to micro-Raman stress mapping has also been reviewed with emphasis on the important cubic semiconductors. <sup>52</sup> Micro-Raman mapping for investigating thermal properties has been reviewed. <sup>53,54</sup>

### III. UV MICRO-RAMAN METHODS

Similar to visible Raman measurement systems, a monochromatic laser excitation source, a spectrometer for dispersing the collected light, a detector, control electronics, and optical components are all necessary elements for obtaining near-UV Raman spectra. For micro-Raman systems, a

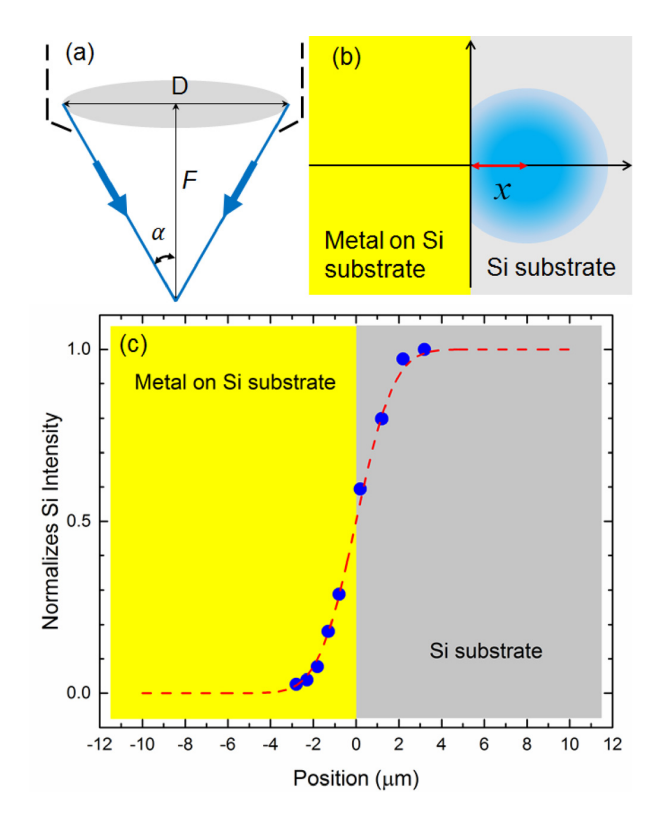


FIG. 1. (a) Defines focal characteristics of the microscope objective. (b) Depicts illuminated silicon area in the standard knife-edge method for determining effective spot size of illumination. (c) Measured intensity versus position and fit used to determine spot size.

microscope is incorporated to focus the laser excitation and collect the backscatter from the test subject. The microscope may be confocal, utilizing a focusing objective with conjugate front- and back-focal points. Alternatively, the microscope design may employ the more common and versatile infinity-corrected focusing objective. Fundamentals and application of micro-Raman imaging have recently been reviewed. We briefly overview here the main components and characteristics that are specific to UV measurements.

Lasers operating in the near UV, and having sufficiently narrow emission lines, are primarily argon (363.8, 351.1 nm), krypton (406.7, 350.7 nm), and helium-cadmium (325.0 nm). Only wavelengths of the main lines in the near UV are listed. The deep-UV range is achievable, for example, by doubling the intense 488.0- or 514.5-nm line from an argon-ion laser. In the wavelength range above 350 nm, standard-grade optical materials are transparent. However, below this wavelength, the optical materials chosen in designing a micro-Raman

instrument become more demanding since they are less transparent in the UV. The attenuation coefficient of laboratory-grade BK-7 glass, for example, increases by a factor of  $\sim 15$  between 363.8 and 325.0 nm. Generally, below 350 nm, specialized UV-grade materials are needed for the optical components of micro-Raman instrumentation.

One of the main advantages of micro-Raman measurements is probing a very small sample or region of a sample. Theoretically, the laser beam focused on a smooth surface using an objective lens with numerical aperture  $NA = n\sin\alpha$ , Fig. 1(a), may be considered to have a diffraction-limited intensity profile with the focal spot approximated by an Airy disk with diameter  $d \sim 1.22 \, \lambda/NA \sim 2.44 \, \lambda_n F/D$ , where  $\lambda_n = \lambda/n$ . In these relations, n is the index of refraction and F and D are the focal length and aperture diameter of the objective lens. This disk locates the first intensity minimum (zero) beyond the central maximum of the circular pattern. Table IV compares this theoretical value for a focusing objective with NA = 0.5 for standard 514.5-nm visible Raman excitation and several near-UV laser wavelengths. The wavelength-dependence of d illustrates one advantage of using UV excitation for these measurements: probing smaller lateral regions of a sample.

Since the actual laser spot size in the micro-Raman instrument is larger than d, due to a variety of practical effects, <sup>63</sup> it is generally characterized experimentally using the knife-edge method. In this technique, an abrupt edge pattern, such as a thin but opaque metallization step, is produced on a smooth and easily measured substrate such as silicon. The metal/silicon edge is translated beneath the illumination spot, as illustrated in Fig. 1(b), and the intensity of the Si  $O(\Gamma)$  phonon line is measured at a series of positions. The intensity of Si is zero when the laser spot is completely over the metal and rises to some maximum when the illumination is over the silicon. The normalized intensity obtained when measuring as a function of knife-edge position x (or position of the beam center from the knife-edge position) is then

$$I(x) = \int_{x'=-x}^{+\infty} \int_{y'=-\infty}^{+\infty} \Phi(x', y') dx' dy', \tag{12}$$

where the intensity function  $\Phi(x',y')$  is the profile of the focused laser. The integration limits take into account only the illuminated portion of the silicon. Since the central diffraction disk of the Airy pattern is approximated well by a Gaussian function, the laser intensity is generally described according to  $\Phi(x') \sim e^{-(x')^2/2\sigma^2}$  where we have restricted our attention to the translation direction of the knife-edge

TABLE IV. Approximate Airy disk diameter d, depth of focus in air, and select media with the index of refraction n, and optical penetration depth in silicon, each at characteristic micro-Raman wavelengths. The numerical aperture NA = 0.5 is assumed.

		Air		Diamond		Silicon		
Wavelength (nm)	Airy d (nm)	Depth of focus (nm)	n <sup>61</sup>	Depth of focus (nm)	n <sup>62</sup>	Depth of focus (nm)	d <sub>opt</sub> (nm) <sup>62</sup>	
514.5	1260	2510	2.4	1050	4.2	600	334	
363.8	890	1780	2.5	710	6.4	280	5.3	
325.0	790	1590	2.5	630	5.1	310	4.0	

method. A measured intensity profile is shown in Fig. 1(c) along with the calculated dependence based on Eq. (12) with  $\sigma = 1.4 \,\mu\text{m}$ . The position-dependent transition of intensity from high to low is then used to evaluate laser spot size. Rather than carrying out the integration of Eq. (12) and working with the resulting error function, numerical differentiation of the measured intensity profile produces a dependence which may be directly compared with the intensity function  $\Phi(x')$ . 63 The resulting  $\sqrt{2}\sigma$  parameter of the normal distribution, where the intensity reduces to 1/e of the maximum, may be used to characterize the focal spot size. Comparing this intensity profile to the Airy disk, by matching the 1/e positions of the two functions, we obtain  $\sigma \sim 0.42 \lambda_n F/D$ . The spatial resolution in the micro-Raman system may now be defined based on various criteria such as Rayleigh<sup>63</sup> using the larger of the Airy or knife-edge spot size. To approach diffraction-limited results, the light is required to fully fill the focusing objective so that D is equal to the full entrance aperture. Otherwise, D must be replaced by the actual diameter of the incident light intensity.

For media that are transparent at a particular Raman wavelength, the depth resolution is related to the beam waist of the light focused by the objective inside the sample with refractive index n. Accordingly, the depth of the focus value is  $\Delta \sim 2dF/D = 4.88 \, \lambda_n F^2/D^2$ . In Table IV, we include the calculated  $\Delta$  at three different wavelengths of interest. These are calculated in air, diamond, and silicon.

In contrast, when the material under study is opaque to the laser excitation, then the optical penetration depth  $(d_{opt})$  is relevant rather than the depth of focus. Because both the excitation and emission are exponentially attenuated,  $d_{opt}$  is written as

$$d_{opt} = 1/(\alpha_L + \alpha_S), \tag{13}$$

where  $\alpha_{L(S)}$  is the optical absorption coefficient at the wavelength of the laser (scattered) light. When the absorption coefficient is a slow function of the wavelength, then this may be approximated  $d_{opt} = 1/2\alpha_L$ . Exploiting the shallow penetration depth of near-UV light to study the near-surface range of select materials is a striking advantage of these Raman measurements. This effect has been previously reported for the study of near-surface Si (e.g., Refs. 64 and 65) and GaN (e.g., Refs. 30 and 66–68), along with detection and study of extremely thin films of SrTiO<sub>3</sub> (e.g., Ref. 69).

Light collected by the microscope consists of Rayleigh and Raman scatter. The former is typically many orders of magnitude stronger than the latter. This makes it essential to discriminate against the intense Rayleigh line. Early work in near-UV micro-Raman relied on multi-stage monochromators which may be used for scanning or multichannel measurements. The advent of holographic notch filters, designed to attenuate a specific laser wavelength while passing the desired nearby range, has resulted in the design of optically fast instrumentation based on single-stage spectrometers. The notch filter attenuation produces a cutoff range from <100 to 200 cm<sup>-1</sup> on either side of the excitation line with some tunability achieved through control of the angle of incidence on the filter. This prohibits the measurement of Raman

bands at wavenumbers below the cutoff. Despite this limitation, most modern Raman instruments are designed with notch filters, single-stage spectrometers, and multichannel detectors with the inherent advantage of high optical throughput.

Instrumental linewidth broadening in Raman measurements is proportional to the slit width, W, and groove spacing of the grating,  $d_G$ , and inversely proportional to the focal length of the spectrometer, f, according to  $\Delta\lambda$  (nm)  $= Wd_G \cos(\theta)/mf$ . Here,  $\theta$  and m represent the diffraction angle and order, respectively. In the small-angle approximation and setting m=1,  $\Delta \lambda \sim W d_G/f$ . For a multichannel detector, such as a charge-coupled device (CCD), positioned in the focal plane of the spectrometer exit, the value of W used is the larger of the entrance slit width of the spectrometer or the corresponding "exit" slit width—nominally twice the pixel size in the dispersive direction (e.g.,  $2 \times 20$  $\mu m = 40 \mu m$ ). In a Raman system using the standard visible laser excitation of 514.5 nm, the spectrometer slit width of  $50 \,\mu\text{m}$ , the focal length of 0.5 m, and the  $1800 \,\text{gr/mm}$  grating, instrumental spectral resolution in wavenumber units is  $\Gamma_{inst}(cm^{-1}) = \frac{\Delta\lambda(nm)}{\lambda^2} = 2 cm^{-1}$ . For otherwise identical conditions when using near-UV excitation, e.g., 363.8 nm, this increases to  $\Gamma_{inst} \sim 4 \, \text{cm}^{-1}$ . Including the (negligible) laser linewidth  $\Gamma_L$ , the total measured linewidth consequently  $\Gamma_{meas} = \sqrt{\Gamma_{ph}^2 + \Gamma_{inst}^2 + \Gamma_L^2} \sim \sqrt{\Gamma_{ph}^2 + \Gamma_{inst}^2}$  for estimating the phonon linewidth, Eq. (8). The latter is often used as an assessment of crystal quality. Approaches for reducing the instrumental impact on the overall linewidth measurement include using higher diffraction orders, gratings with higher groove density, or a spectrometer with a greater focal length.

A final desired element of micro-Raman work is the possibility of mapping various dependences across a sample surface. Translation stages may be manual or automated to conduct the measurement at desired x and y locations. Automated stages are available with order 0.1- $\mu$ m step resolution for mapping of various parameters with particular interest devoted to stress or temperature distributions.

# IV. STRESS AND COMPOSITION IN SILICON AND RELATED MATERIALS

Fabrication of silicon electronics requires integration of numerous materials, having a wide range of dimensions, to produce three-dimensional device structures. Stress and strain may be classified as processing-induced and engineered to influence carrier transport properties. The former arises from the elevated temperatures used to deposit and control the myriad necessary electronic materials in device architectures. These processes give rise to stress from lattice mismatch and differential thermal expansion. These factors are influenced by processing parameters but are otherwise unavoidable. In contrast, strain may be intentionally designed to modify carrier transport, e.g., in p-type metaloxide-semiconductor (p-MOS) transistors. 70-74 Stress issues are enhanced when feature sizes shrink, thereby making it crucial to measure and map local stresses. One prominent demonstration of micro-Raman mapping is to investigate the

stresses induced in silicon due to fabrication of integrated circuits<sup>52</sup> including UV micro-Raman studies.<sup>22,75–80</sup>

As mentioned above, the spatial resolution in a near-diffraction-limited Raman-microprobe is on the order of, and in proportion to, the excitation wavelength. This produces a modest advantage in mapping stresses in silicon device structures. Because the bandgap of silicon is indirect below  $\sim$ 3.4 eV, it is a relatively weak light absorber. Therefore, a stronger motivation to conduct UV micro-Raman investigations comes from considering the optical penetration depth in silicon. Figure 2 shows the absorption coefficient ( $\alpha$ ) versus photon energy obtained from spectroscopic ellipsometry measurements of the dielectric function.<sup>62</sup> Using Eq. (13), we may estimate  $d_{opt}$  from these data. For visible Raman scattering at 514.5 nm, we obtain  $d_{opt} \sim 340$  nm. These measurements provide an average property over a depth which is not generally representative of the shallow active regions in silicon electronics. Excitation energy >3.4 eV, on the other hand, is above the direct  $E_1$  transition in silicon. At a UV excitation wavelength of 351.1 nm, the corresponding  $d_{opt}$  $\sim 5\,\mathrm{nm}$  is ideal for studying shallow structures in silicon integrated circuits. The use of ultraviolet (UV) excitation in Raman stress mapping studies has the major advantage of probing significantly shallower depths.

The first application of UV micro-Raman to map lateral stress variations in silicon was reported by Holtz *et al.* using 350.7-nm excitation from a Kr-ion laser. <sup>64</sup> Rather than using a notch filter, they used a f = 0.85-m double monochromator for light dispersion and CCD for multichannel detection. Shifts as small as  $0.07 \, \mathrm{cm}^{-1}$  were measured corresponding to stresses on the order of 35 MPa.

Figure 3(a) shows the patterned material stack investigated. Area patterns were on the 10- and 20- $\mu$ m scales. The area imaged is depicted by the dashed lines. Shown in Fig. 3(b) is the position dependence of the change in the Raman peak energy from that of device silicon. Under the

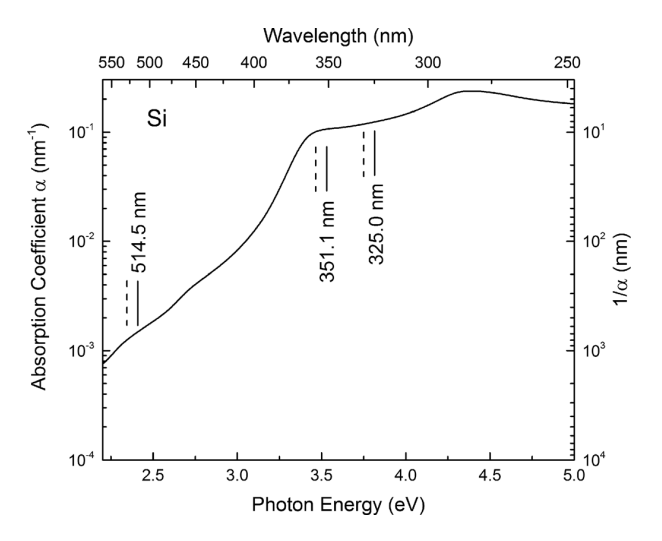
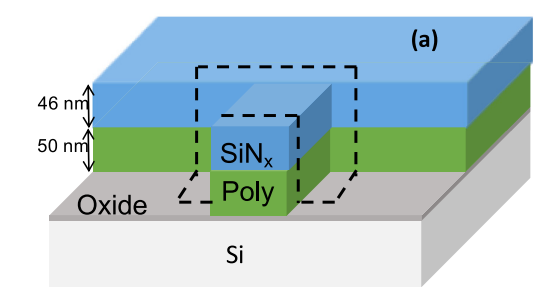


FIG. 2. Absorption coefficient of silicon vs photon energy. Indicated on the right-hand axis is the corresponding  $1/\alpha$ . Several standard Raman excitation wavelengths are included as solid vertical lines. The dashed lines correspond to the Raman shift due to scattering by the silicon  $O(\Gamma)$  phonon. The dependence is calculated using published spectroscopic ellipsometry data. 62



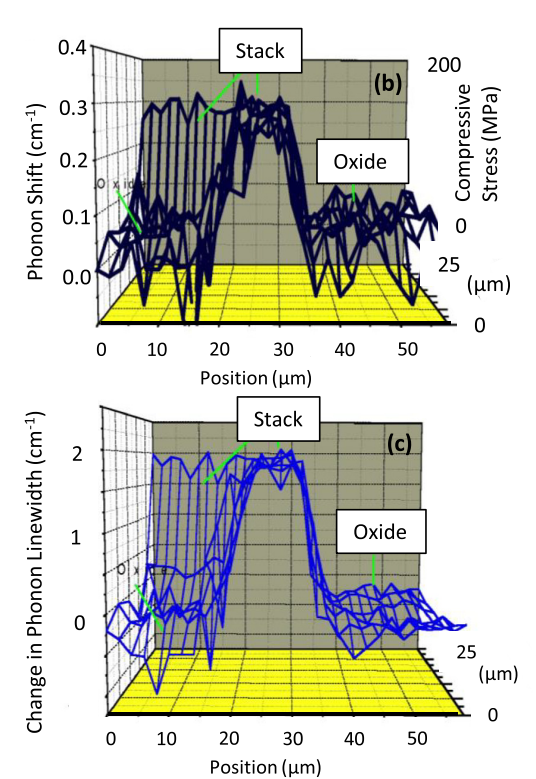


FIG. 3. (a) Patterned material stack investigated using 350.7-nm excitation. The region in dashed lines is imaged on the right-hand data. Clearly seen is a shift in (b) the silicon phonon energy due to stress from the oxide and (c) an elevated linewidth in the polycrystalline silicon. Reproduced with permission from Appl. Phys. Lett. **74**, 2008–2010 (1999). Copyright 1999 AIP Publishing LLC.

stack, a characteristic blueshift is observed in the polycrystalline silicon (Poly) corresponding to ~140 MPa of compressive stress (right-hand vertical scale). The origins of this stress are thermal expansion mismatches between the poly and oxide, as well as nitride layer, and intrinsic stress within the poly due to grain formation. Figure 3(c) shows the image obtained by analyzing the phonon linewidth broadening in the poly relative to that in device-quality silicon. The broadening observed in the Poly material was attributed to crystallite size, orientation, and stress variations. Changes in phonon energy and linewidth thus provide consistent images from this material stack.

This demonstration was soon followed by a report from Dombrowski *et al.*,  $^{67}$  who investigated stress in a 3- $\mu$ m wide test structure. The sample was composed of a 200-nm thick SiN<sub>x</sub> on Si that was pattern etched slightly into the silicon

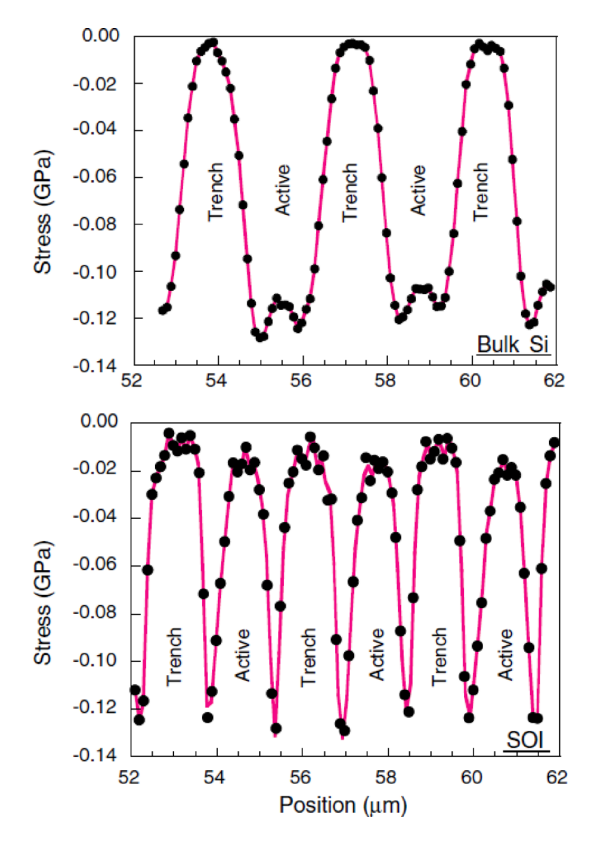


FIG. 4. Stress variation obtained by the UV-Raman (325 nm) 1-D line scan of STI test structures with a 1.5  $\mu$ m width. The upper panel is prepared using bulk Si and the lower with SOI. Reproduced with permission from AIP Conf. Proc. **683**(1), 738–743 (2003). Copyright 2003 AIP Publishing LLC.

wafer to produce a raised  $SiN_x/Si$  stripe on Si. This was blanket coated with a 600-nm thick oxide layer. The 363.8-nm laser line was used for excitation. The resulting map showed compressive stress beneath  $SiN_x$  in excess of 0.4 GPa and significant compressive pinching near the stripe edge as high as 0.9 GPa.

One of the principal areas where UV Raman stress mapping has been applied is in shallow trench isolation (STI) in silicon.  $^{22,75-78,80}$  In this approach, a micron "deep" trench is etched in the silicon and subsequently lined and filled with  $\mathrm{SiO}_2$  to electrically isolate neighboring devices. It is advantageous to have the trenches as narrow as possible for

maximizing available device footprint. The two dissimilar materials, Si and SiO<sub>2</sub>, result in high thermal stresses. Liu and Canonico used (325-nm) UV micro-Raman to map the stress in STI for complementary MOS (CMOS) technology. The laser illumination is focused to  $\sim$ 0.43  $\mu$ m using an objective with NA=0.9, and a double monochromator dispersed the spectrum. They investigated different sizes of STI structures fabricated on bulk Si and silicon-on-insulator (SOI) substrates after trench oxide deposition. The representative results are shown in Fig. 4. The trench regions are found to be nearly relaxed with maximum stress near the edges of the active regions. Stresses in the active regions are found to be compressive, reaching a magnitude of  $\sim$ 0.12 GPa in the result shown and a maximum magnitude of  $\sim$ 0.16 GPa for smaller structures.

Ogura and co-workers extended the approach to investigate pattern-induced strain in SOI.<sup>65</sup> Several prototype structures were examined, each serving as a representative MOS situation. The authors implemented an innovative approach for generating a pseudo-line image by actuation of a singleaxis scanning mirror to raster the laser focus across the sample while capturing open aperture images at 200-nm intervals. Several visible and UV wavelengths were investigated. Due to enhancement of the Raman process via resonance with the direct  $E_1$  transition in silicon, they conclude that the 363.8-nm excitation wavelength is best for obtaining good scattering intensity at laser power sufficiently low to obviate local heating. Figure 5(a) shows micro-Raman data for the SOI silicon shift induced by a patterned SiN<sub>x</sub> layer, 80 nm thick, obtained using visible and near-UV excitation. In both cases, enhanced compression (blueshift) is observed beneath the edge of SiN<sub>x</sub>, and a tensile stress (red shift) reaction is seen beneath the openings in the layer, presumably relative to the SOI silicon phonon energy far from the pattern. Reducing the opening size increases the observed tensile stress as compressive forces from the SiN<sub>x</sub> edges combine to pinch the SOI layer. Notably, the data beautifully illustrate the importance of using the excitation wavelength to match the needed probe depth for interrogating stress within the affected near-surface region of interest.

The optical penetration depth in UV Raman has also been exploited to investigate the effects of ultra-shallow ion implantation in silicon<sup>81,82</sup> and 4H-SiC.<sup>83</sup> O'Reilly *et al.* 

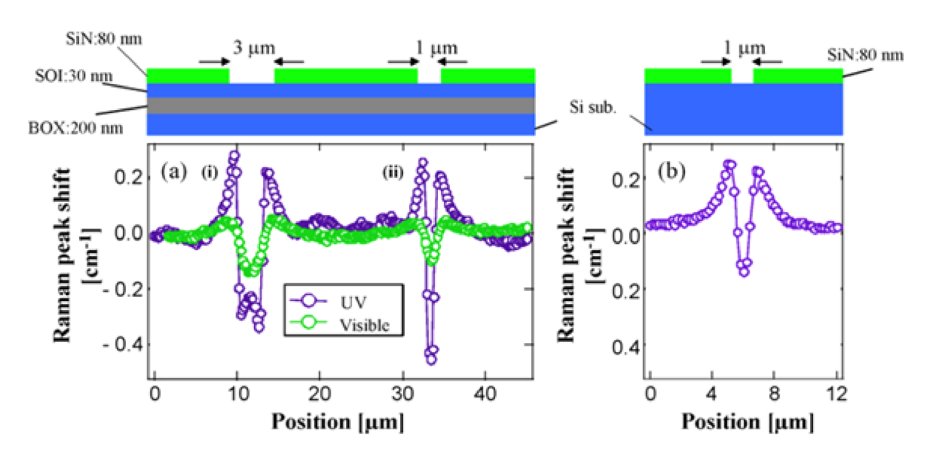


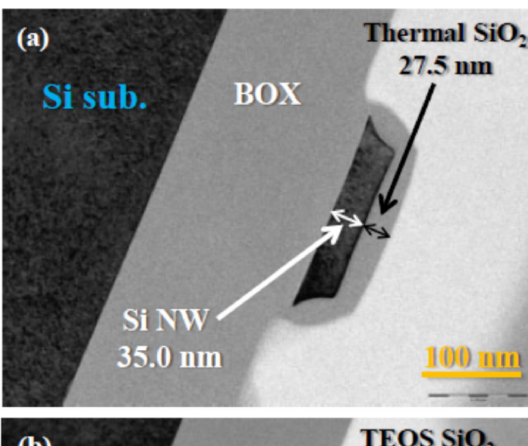
FIG. 5. One-dimensional image of stress-induced Raman shift in (a) SOI due to the patterned  $\mathrm{SiN}_x$  layer depicted and (b) directly patterned on silicon. Data for visible (532 nm) and UV (363.8 nm) excitation are shown. Reprinted with permission from Ogura et al., Mater. Sci. Eng., B **159–160**, 206–211 (2009). Copyright 2009 Elsevier.

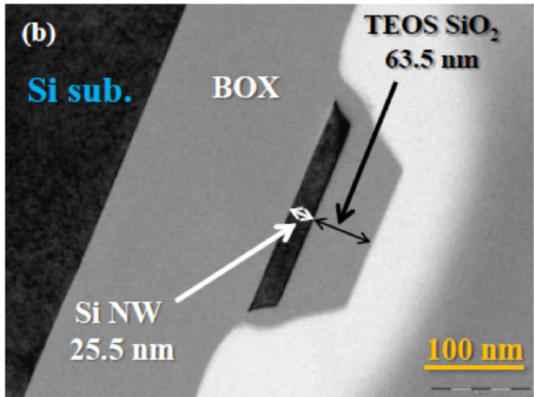
reported UV micro-Raman with 325-nm excitation and reciprocal-space maps (RSMs) from high-resolution X-ray diffraction (HRXRD) studies of antimony-implanted silicon prior and post anneal.81 The silicon was grown epitaxially on silicon-germanium to produce a biaxial tensile strain in the former. The implant was done at low energy, 2 keV, for producing a junction depth of  $\sim 10 \,\mathrm{nm}$ . Post-implantation, a phonon red shift is observed which is correlated with the tensile strain. Annealing produces a greater red shift that, according to the HRXRD, is not related to strain. The authors observe a correlation with the doping concentration which was interpreted as softening of the phonon deformation potential.<sup>84</sup> Although it is necessary to differentiate between the effects of local stress and doping levels in excess of  $5 \times 10^{19} \,\mathrm{cm}^{-3}$ , the authors conclude that UV micro-Raman measurements are potentially useful for mapping the carrier concentration.81

To investigate separating effects of strain and doping, Lee *et al.* studied heavily phosphorous-doped silicon grown epitaxially on silicon substrates. The epitaxial layer was ~65 nm thick so that 532-nm visible micro-Raman measurements were dominated by scatter from the underlying substrate. When implementing 325-nm UV excitation, only the epitaxial film is probed and a systematic red shift is reported with the increasing P concentration up to 6 at. %. To extract the portion of the shift due to the composition, the authors calculate the strain contribution which is observed to be dominant. The linear dependence of the strain-induced shift was corroborated using HRXRD measurements and found to be valid over this concentration range.

We close the discussion of UV micro-Raman mapping in silicon with a recent report by Ryo et al. 86 examining strain in silicon nanowires. The nanowires were prepared using SOI as the starting material. Electron-beam lithography and a subtractive process were used to produce the nanowires which were encapsulated by silicon oxide using solely a thermal oxidation step or by first incorporating a lowtemperature tetra-ethyl orthosilicate (TEOS) layer, prior to patterning, and a thermal oxide. The wires were shown to be 25-35 nm thick and approximately 220-nm wide, as seen in Figs. 6(a) and 6(b). Successful determination of stress in these nanowires relies on shallow optical penetration and lateral spatial resolution approaching the width. The authors used 355-nm excitation from a frequency-tripled Nd:YAG laser and a 2.0-m focal length spectrometer to disperse the light while stepping the position of the sample at 100-nm intervals to obtain a line map. Despite the ~650-nm focus diameter being substantially larger than the nanowire width, Fig. 6(c) clearly illustrates the observed red shift (tensile stress) on the silicon and a compressive reaction stress on the Si substrate through the 200-nm thick buried oxide (BOX) layer.

Semiconductor alloys, such as  $Si_{1-x}Ge_x$ , where x is the germanium mole fraction, have been used for intentionally introducing strain in p-MOS active regions in silicon electronics. <sup>70–74,87–89</sup> An important consideration in the growth of  $Si_{1-x}Ge_x$  alloys on silicon substrates is the presence of lattice mismatch strain, as discussed in Sec. II. Since pure germanium has a lattice constant,  $\sim$ 4% larger than that of





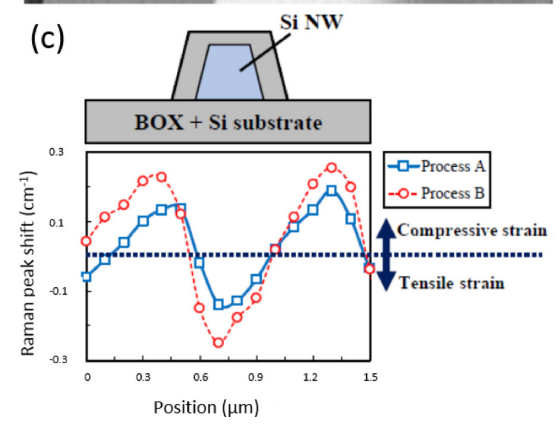


FIG. 6. Silicon nanowires prepared by a subtractive process beginning with SOI wafers. (a) and (b) TEM cross-sections for processes without and with, respectively, a TEOS oxide layer prior to etch removal of the silicon. (c) The Raman phonon shift versus position across the nanowire. The *figure* is reproduced with permission from Ryo *et al.*, Jpn. J. Appl. Phys., Part 1 **56**(6S1), 06GG10 (2017). Copyright 2017 The Japan Society of Applied Physics.

silicon, and the lattice constant increases monotonically with the composition according to Vegard's law, thin epitaxial alloy layers will be under biaxial compressive strain. If layers are grown exceeding a certain critical thickness, the strain relaxes by producing line dislocations. The latter is deleterious to device performance.

Holtz *et al.* used UV Raman measurements, with the excitation wavelength varying from 350.7 nm to 514.5 nm, to study  $Si_{1-x}Ge_x$  alloys grown on the Si substrate. <sup>91</sup> Samples grown by organo-metallic chemical vapor deposition

(OMCVD) were  $1-2 \, \mu m$  thick and confirmed by X-ray diffraction to be strain relaxed. Layers grown by molecular-beam epitaxy (MBE) were thin and pseudomorphically strained. The near-UV Raman measurements allow isolation of the spectrum from each  $Si_{1-x}Ge_x$  alloy, including the thin MBE layers.

Figure 7(a) demonstrates the effect of the optical penetration depth on the Raman spectra for the MBE-grown samples with x=22% and thickness 55 nm. <sup>91</sup> The spectra were obtained using four excitation wavelengths. When using 514.5 nm excitation, the spectrum is dominated by the silicon substrate optic phonon  $O(\Gamma)$  at  $520 \, \mathrm{cm}^{-1}$ . The corresponding alloy Si–Si phonon, seen near  $513 \, \mathrm{cm}^{-1}$ , is a shoulder in this spectrum. As the wavelength is tuned into the deep blue (457.9 nm) and near UV (413.1 nm), the relative intensities shift to being less dominated by the substrate with stronger  $\mathrm{Si}_{1-x}\mathrm{Ge}_x$  alloy scatter. At 351 nm, only the epilayer band is observed, with no scatter seen from the substrate. For the spectra in which both the alloy and substrate band are observed, the relative intensities are described according to

wavelength-dependent attenuation and layer thickness. Figure 7(b) shows Raman spectra of samples grown by MBE with varying *x*. The spectra were obtained by 350.7-nm excitation so that only bands from the epi-layer are measured. The spectra in Fig. 7(b) illustrate the expected consistent redshift of the Si-Si phonon energy with the increasing Ge composition.

Figure 7(c) summarizes the composition dependence shift in the Si-Si phonon energy from that of pure bulk Si obtained for all samples studied in Ref. 91. Since samples grown by OMCVD are fully relaxed, the dash-dotted linear fit to those data points describes the composition-dependent unstrained phonon energy (cm<sup>-1</sup>) and is found to be  $\omega_0(x) = 520.0 - 68x$ . The dashed line in Fig. 7(c) is a linear fit to data obtained from samples grown by MBE with a slope  $d\omega/dx = -30.7 \pm 0.6$  cm<sup>-1</sup>, which is a combination of alloying (dashed-dotted line) and strain effects. The solid line in Fig. 7(c) represents the combination of alloying and strain using published phonon deformation potentials as described in Ref. 91. Figure 7(d) shows the strain-only shift in Si-Si

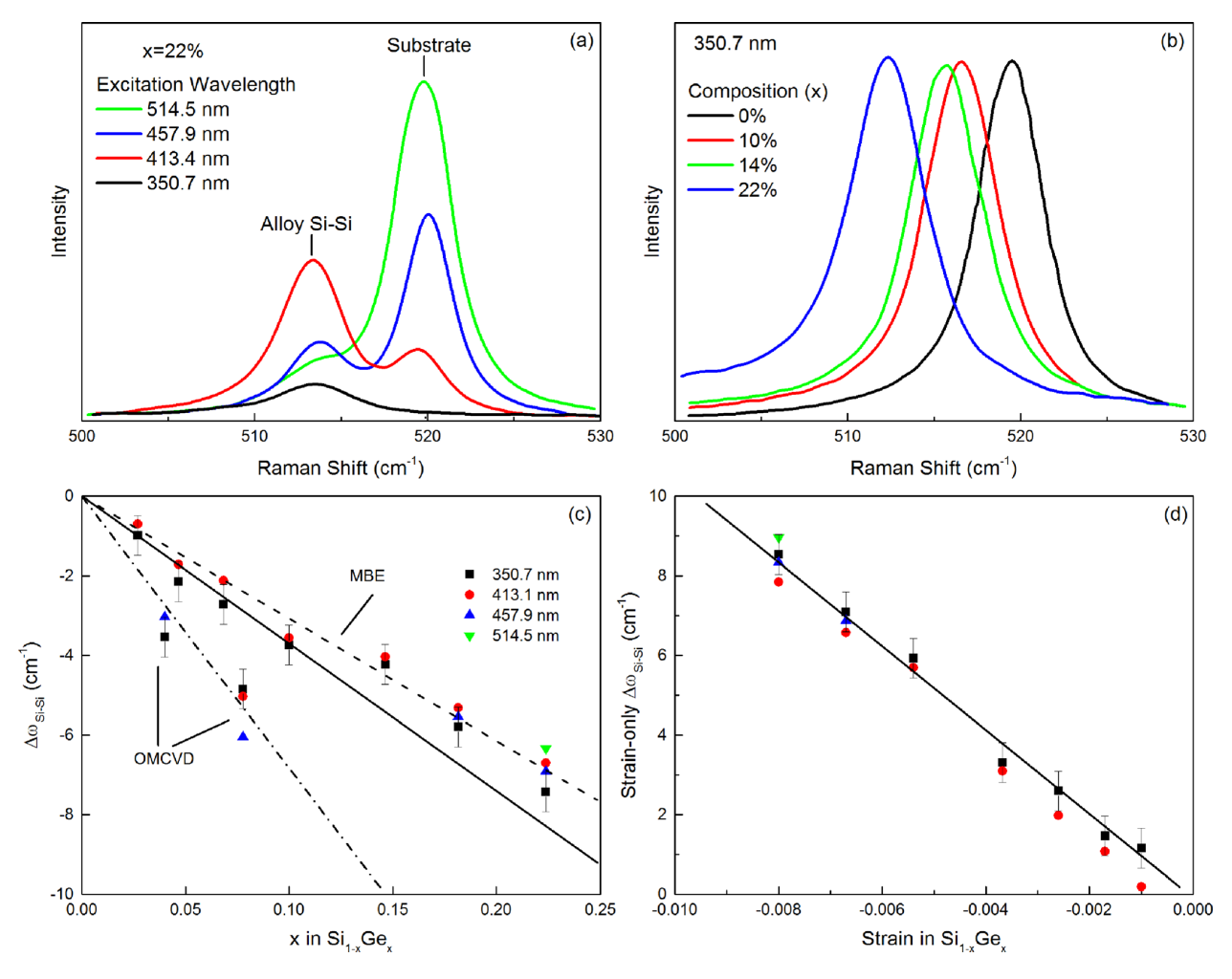


FIG. 7. (a) Raman spectra excited using several wavelengths for a 55-nm thick  $\mathrm{Si}_{1-x}\mathrm{Ge}_x$  alloy (x=0.22) grown by MBE. (b) Normalized Raman spectra for various MBE grown epilayers excited by 351 nm light. Ge composition values x in  $\mathrm{Si}_{1-x}\mathrm{Ge}_x$  are noted. (c) Summary data of the shift in the Si–Si phonon energy, from that of bulk silicon, versus x. OMCVD samples are strain-relaxed epilayers. MBE epilayers are fully (pseudomorphically) strained. (d) Summary data of the shift of the Si–Si phonon energy for the MBE-grown films with the effect of alloying (dash-dotted line:  $\omega_0(x) = 520.0 - 68x$ ) subtracted. Reproduced with permission from J. Appl. Phys. **88**, 2523 (2000). Copyright 2000 AIP Publishing LLC.

phonon versus in-plane lattice-mismatch strain,  $\varepsilon_{\parallel}(x) = \frac{a_{Si} - a(x)}{a(x)}$ , where  $a_{Si}$  and a(x) are lattice constants of the silicon substrate and unstrained alloy. The combined studies of fully relaxed and pseudomorphically strained  $\mathrm{Si}_{1-x}\mathrm{Ge}_x$  alloys, with the near-UV measurement of the thinnest epitaxial layers, permit determination of both alloy- and strain-only effects.

# V. STRESS AND THERMAL PROPERTIES OF GROUP-III-NITRIDE MATERIALS AND DEVICES

One important application of Raman spectroscopy is found in the early development of III-nitride semiconductors and understanding growth-related determining stresses. 34,35,92-95 The primary cause for stresses in these materials is the ubiquitous need to grow the III-nitride semiconductors on non-native substrates such as sapphire, silicon carbide, and silicon. Stresses subsequently arise from lattice mismatch and differences in the CTE between the layers during high-temperature processing. 92 Concerns related to stress include layer cracking, 96 wafer bow or warping, 97 and changes in the electrical behavior of devices. 98,99 Subsequent processing and development steps, such as the deposition of adhesion/passivation layers (e.g., SiO<sub>2</sub> and SiN<sub>x</sub>), also contribute additional stresses to the epitaxial layers.

Thermal management in electronics is currently the principal barrier for decreasing the device component size and increasing power densities. This is particularly the case in AlGaN/GaN high electron mobility transistors (HEMTs) where current flows within the <10-nm thick twodimensional electron gas (2DEG) that forms spontaneously at the interface between the GaN and AlGaN barrier. When a source-drain voltage is applied, confinement of the current to the 2DEG creates extreme current crowding. The ensuing self-heating produces localized temperature rises as high as 350 °C, <sup>68</sup> particularly at the gate edge where a power spike occurs. Efforts for improving heat extraction from the active region, such as incorporation of substrates with high thermal conductivity, have shown substantial promise for thermal management. 100,101 We return later to diamond as a potential material for passive thermal management applications.

Basics of the micro-Raman temperature measurement have been described in Sec. II. Here, we focus on near-UV micro-Raman studies of self-heating in HEMT and other devices and the effects of integrating GaN with diamond for thermal management.

One approach for depth profiling temperature rises in transparent materials is the use of confocal micro-Raman measurements. The near-surface material (GaN) is emphasized by focusing the confocal apparatus  $\sim 1-\mu m$  above the actual sample surface so that the tail of the beam waist gives appreciable Raman scatter. Alternatively, the optical penetration depth can be tuned via the choice of excitation source. This tuning provides an elegant approach to study the very shallow depth or entire thickness of select materials.  $^{34,66-68}$  Figure 8 shows absorption coefficient versus photon energy calculated using published spectroscopic ellipsometry data. When carrying out near-UV

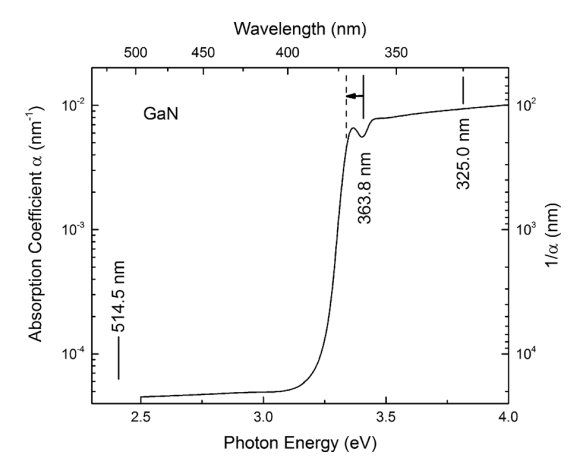


FIG. 8. Absorption coefficient for GaN calculated from ellipsometry data. <sup>103</sup>
The right-hand axis shows 1/α.

measurements of GaN, e.g., using 363.8-nm excitation, it is also important to consider stress- and temperature-induced shifts in the energy gap which affect the rapidly varying absorption coefficient. These may be taken into account, over a small range, by rigidly shifting the absorption spectrum according to established stress<sup>92</sup> and temperature<sup>57</sup> coefficients. Another factor to consider is the strong photoluminescence from the GaN, which is generally far stronger than the Raman scatter even under resonant or near-resonant conditions. Even with these constraints, this excitation source has been used to investigate shallow depths within the AlGaN HEMT.<sup>66–68</sup>

The first such UV micro-Raman study combined measurements with (visible) 488.0 nm and 363.8 nm excitation to examine self-heating in an AlGaN/GaN HEMT device grown on a 6*H*-SiC substrate. <sup>66</sup> For an input power of 3 W/mm and zero gate voltage, temperature rise from room temperature close to the 2DEG, in the GaN buffer layer, and the 6*H*-SiC substrate is obtained at 130, 55, and 15 °C, respectively. Results were interpreted based on coordinated electrical and thermal simulations.

More recently, Nazari *et al.* capitalized on the material-specific phonon energies in Raman spectra for depth profiling temperature rise in a HEMT stack, as illustrated in Fig.  $9.^{68}$  The use of micro-Raman spectroscopy to examine a transparent multilayer stack is beautifully illustrated in the visible spectra presented in Fig. 9(a). A TEM cross-section of the material stack is shown in the inset. Phonons are observed from the GaN, AlGaN transition layers (TL), AlN, and Si substrate. Temperature rise is generally estimated based on the  $E_2^2$ -symmetry phonon of the wurtzite crystal structure. Also shown in Fig. 9(b) are the GaN (only) phonons observed when measuring with 363.8-nm excitation. Under device drive conditions, these combined measurements permit the simultaneous study of temperature rise in each material layer.  $^{68}$ 

Combining the phonon redshift obtained from visible and UV measurements, Nazari *et al.* established a temperature depth profile.<sup>68</sup> Figure 9(c) shows such a profile for input powers of 2.6 and 7.8 W/mm at zero gate voltage.

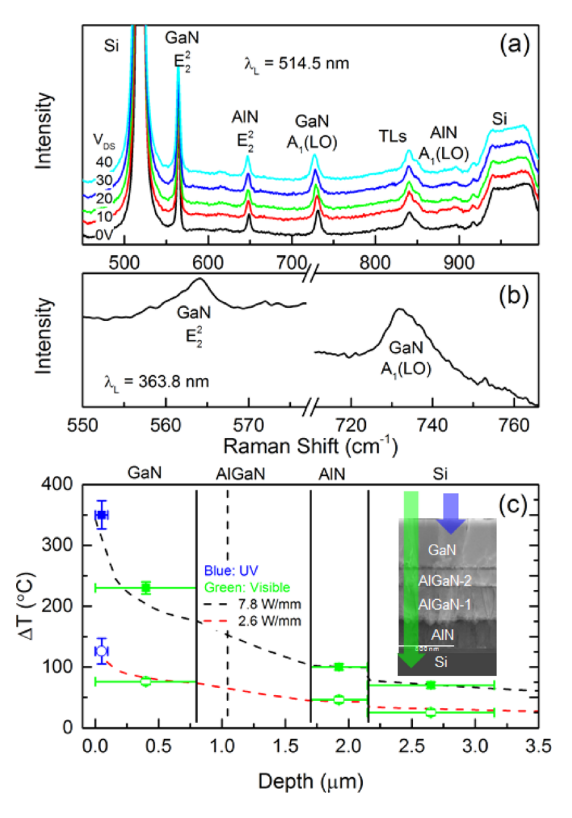


FIG. 9. (a) Visible Raman spectra of the AlGaN/GaN HEMT taken at different drain-source voltages with zero gate bias. Raman features are observed from the substrate, AlN, transition layers, and GaN. (b) UV Raman spectrum of the device at  $V_{\rm DS}=0$  ( $V_{\rm GS}=0$ ) showing  $E_2^2$  and  $A_1({\rm LO})$  phonons. In the UV spectra, the background photoluminescence from GaN is approximately ten times the intensity of the Raman bands. (c) Temperature rise in different parts of the AlGaN/GaN heterostructure at two different input powers obtained from Raman measurements (data points) along with representative FE thermal simulations (dashed). Black and red (dashed) correspond to temperature rises in the device for input powers of  $\sim$ 7.8 and 2.6 W/mm, respectively. Vertical solid lines separate different layers in the device, and the vertical dashed line separates two AlGaN transition layers. The inset shows TEM cross-section of HEMT with the probe depth of UV and visible excitation depicted. Reprinted with permission from Nazari et al., IEEE Trans. Electron Devices 62(5), 1467–1472 (2015). Copyright 2015 IEEE.

Temperature rise due to self-heating in a small region  $(\sim 100 \,\mathrm{nm})$  around the 2DEG is significant and measured at  $\sim$ 340 °C for 7.8 W/mm of input power. This is almost twice as high as the average temperature increase in the GaN buffer layer obtained from visible micro-Raman under identical conditions, thereby illustrating the importance of the UV measurements. The temperature rises for the AlN nucleation layer and Si substrate are  $\sim 100$  and 60 °C, respectively, under the same input power. The temperature rises are found to be approximately linearly on input power up to the maximum 8 W/mm studied here. The results are interpreted based on a 3D finite element simulation. Good agreement between the measured and the simulated temperature rise in different layers is obtained using literature values of thermal conductivities and one thermal boundary resistance (TBR) at the interface between AlN and Si with value  $1 \times 10^{-8}$  K m<sup>2</sup>/W.

Thermal management in high-power light emitting diodes (LEDs), based on the III-nitrides, is also critical for increasing output powers and device life spans. Alarcón-

Lladó et al. have used near-UV micro-Raman measurements to examine temperature rise in an InGaN/GaN vertical LED which was transferred to a 150-µm thick copper substrate for establishing direct thermal contact [Fig. 10(a)]. 104 As seen in the Raman spectra of Fig. 10(b), the  $E_2^2(E_{2h})$  phonon is sensitive to drive conditions and may therefore be used to estimate temperature rise in the topmost GaN layer of the device stack. This is shown in Fig. 10(c) versus drive current. When the 1-mm<sup>2</sup> device is driven at 1 A, corresponding to an input power of 6 W, they directly measure a temperature rise  $\Delta T = 200$  °C near the contact electrode where the greatest effect is expected due to current crowding. The authors demonstrate effectively the usefulness of the measurement in obtaining accurate temperature characterization of the device structure through a smooth dependence of  $\Delta T$  even at low drive currents.

An approach aimed at passive thermal management is integration of diamond with semiconductor devices prone to excessive self-heating. Diamond has exceptional thermal conductivity making it a promising material for use with GaN-based HEMTs. A key concern in this integration processing is the stress produced by the high-temperature steps of either bonding or direct CVD growth of diamond on GaN. Hancock *et al.* investigated stress in the 730-nm thick GaN

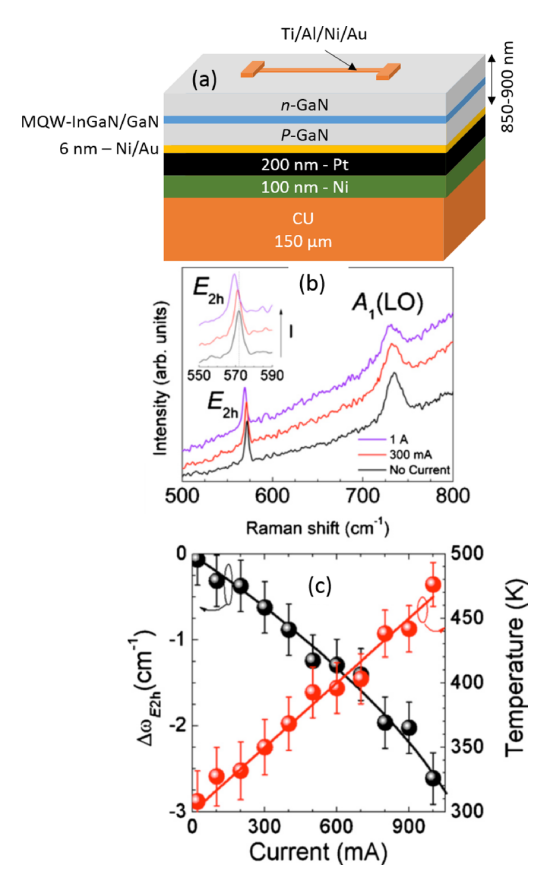


FIG. 10. (a) Depicts LED structure post transfer to copper heat sink substrate. (b) Near UV (325 nm) Raman spectra of the topmost GaN layer under different LED drive currents. (c) Phonon shift and corresponding absolute temperature in the GaN. Reproduced with permission from J. Appl. Phys. **108**(11), 114501 (2010). Copyright 2010 AIP Publishing LLC.

layer of a 100-mm diameter AlGaN-based HEMT stack following CVD growth of a 100- $\mu$ m thick diamond layer. Stresses  $\sigma_{xx}$  in the GaN layer are estimated based on shifts in the Raman-active  $E_2^2$ -symmetry phonon;  $^{34,92,97}$  see Table II. Combining visible (514.5 nm) and near UV (363.8 nm) micro-Raman, respective values were obtained for *volume average* and *near-surface* (100–130 nm) stress on the GaN layer. Near-UV micro-Raman measurements were carried out from the exposed surface (denoted GaN side) and through the transparent diamond at the diamond/GaN interface (denoted GaN/D side). As a bonus, the visible measurements also provide the stress measurement in the diamond. The results shown in Figs. 11(a) and 11(b) reveal an unexpected stress gradient in the GaN.

Full-wafer stress maps showed remarkable uniformity.  $^{30,105}$  The average stress measured from the visible micro-Raman was  $\sigma_{ave}=0.32$  GPa with uncertainty values of individual data points  $\pm 0.06$  GPa and cross-wafer variance (standard deviation) of 0.10 GPa from the map. The near-UV measurements show the tensile stress in the GaN-side with an average value  $\sigma_{GaN}=0.86$  GPa. For the GaN/D side, the tensile stress has an average value  $\sigma_{GaN/D}=0.23$  GPa. This counterintuitive stress gradient is attributed to local (nanoscale) relaxation  $^{97}$  immediately surrounding the ubiquitous threading dislocations (TDs) in the GaN and a variation in the density of the TDs along the GaN growth axis.

To simulate the stress profile in the GaN layer, while taking into account the TD density, the effective elastic modulus of the GaN layer is modified according to

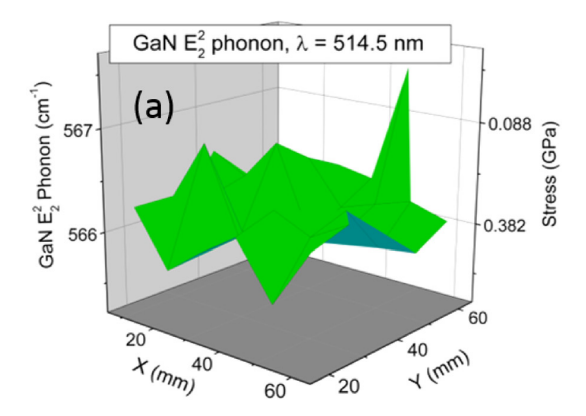
$$E_{GaN}^{eff} = (1 - f)E_{GaN}^{bulk},\tag{14}$$

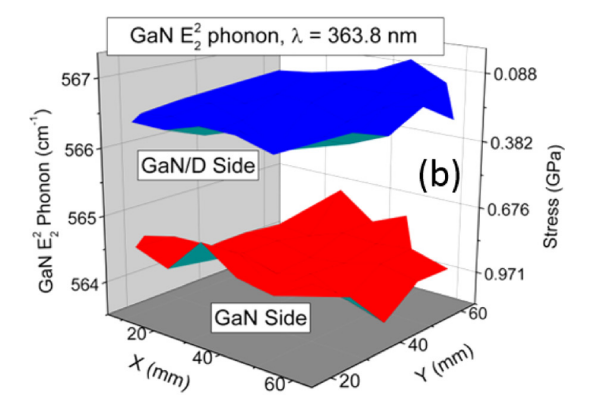
where  $E_{GaN}^{bulk}$  is the elastic modulus for bulk GaN<sup>106</sup> and  $f=nL^2$  is the average relaxation factor with characteristic length-scale L, and n represents the TD areal density. The presence of TDs is confirmed using bright-field TEM imaging with two estimated values of  $1\times 10^9~{\rm cm}^{-2}$  and  $9\times 10^9~{\rm cm}^{-2}$  for the GaN and GaN/D portions of the layer, respectively. A two-region model with three fitting parameters ( $f_{GaN}$ ,  $f_{GaN/D}$ , and either  $t_1$  or  $t_2$  due to the constraint  $t_1+t_2=t=730~{\rm nm}$ ) is used. Two stress values obtained from the UV ( $\sigma_{GaN}$  and  $\sigma_{GaN/D}$ ) plus the average stress ( $\sigma_{ave}$ ) from visible micro-Raman measurements can be used to estimate  $t_1$  (and  $t_2$ ) according to

$$\sigma_{ave} = (t_1 \sigma_{GaN} + t_2 \sigma_{GaN/D}) / (t_1 + t_2).$$
 (15)

From this, we determine  $t_1 = 100 \pm 10$  nm and  $t_2 = 630 \pm 90$  nm. Using these values, and incorporating Young's modulus from Eq. (14), the stress cross-section may be simulated to determine the remaining unknown relaxation factors  $f_{GaN}$  and  $f_{GaN/D}$ .

Figure 11(c) presents the resulting simulated  $\sigma_{xx}$  and measured values as a function of the vertical material cross-section. The simulated stress is shown as a dashed line. The measured stress values from visible and UV micro-Raman, for each side of the wafer, are represented as patterned rectangles with the vertical dimension corresponding to standard deviations and horizontal dimension the depth optically





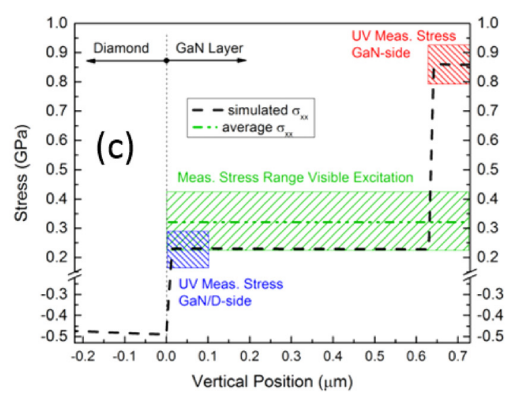


FIG. 11. (a) Visible Raman map for  $GaN E_2^2$  phonon energy. (b) Map of the  $GaN E_2^2$  phonon energy from UV micro-Raman measurements. The upper (lower) surface manifold corresponds to the measurement from the GaN/D (GaN) side of the wafer. The right-hand axis in both graphs shows the stresses obtained from each measurement. (c) Results from FE simulation (dashed lines) of stress as a function of the cross-section distance from the GaN/D interface. The measured stress values from visible and UV micro-Raman, for each side of the wafer, are represented as patterned rectangles. The vertical dimensions correspond to standard deviations from data and horizontal dimensions the optical probe depth for each measurement. Reproduced from with permission from Appl. Phys. Lett. 108(21), 211901 (2016). Copyright 2016 AIP Publishing LLC.

probed for each measurement. The abrupt shape of this dependence is due to the simple two-region model used here. Good agreement with the measured stress is obtained using relaxation factors of  $f_{GaN/D} = 0.76$  in the GaN close to the GaN/D interface and  $f_{GaN} = 0.095$  near the AlGaN-GaN interface. Understanding the stress profile was made possible

by the combined visible and near-UV measurements, with the latter most sensitive to the surface or interface properties.

# **VI. CARBON**

Raman spectroscopy has long served as a premier method for investigating the diverse forms of pure carbon. These include diamond, graphite, graphene, nanotubes, fullerenes, and various structures of amorphous carbon. 9,10,18,25,54,107–113 Here, we focus on applications of UV Raman to the study of these materials.

A broad range of wavelengths, including UV, has been used to conduct Raman studies of graphite. 10 One success of this multispectral approach was to understand a previously long-reported, systematic variation in the peak position of the so-called D mode of graphite. This mode is related to the finite size in graphite layers which allows non-zone-center phonons to participate in first-order Raman scattering. By examining data based on excitation energies ranging from  $\sim$ 1.5 to 3.5 eV (Fig. 12), Thomsen and Reich observed shifts in the D band  $\sim 60 \,\mathrm{cm}^{-1}/\mathrm{eV}$ . They invoke a doubleresonance effect involving the (~linear-dispersion) energy bands of graphite. The excitation energy promotes electrons into unique k values within the Brillouin zone. A phonon scatters the electron into a second energy band, in another region of the Brillouin zone. Inelastic scattering then returns the electron close to the initial k value prior to the recombination (Stokes scatter). The unique wavevector range of the initial absorption requires the disorder-related phonon scattering to possess similarly unique energy. In a subsequent article, these unique energies were successfully mapped onto the phonon dispersion of graphite. 114

The Raman peak position, linewidth, and intensity are shown to depend on the number of layers in the two-dimensional structure of graphene. The Raman G and 2D (also known as G') bands in graphene red shift and blue shift, respectively, as the number of layers increased. The position of either the G or the 2D band can therefore be used in graphene to estimate the number of layers present. The relative Raman intensity of the G line to the 2D line,  $I_G/I_{2D}$ , depends on the number of layers (n) present.

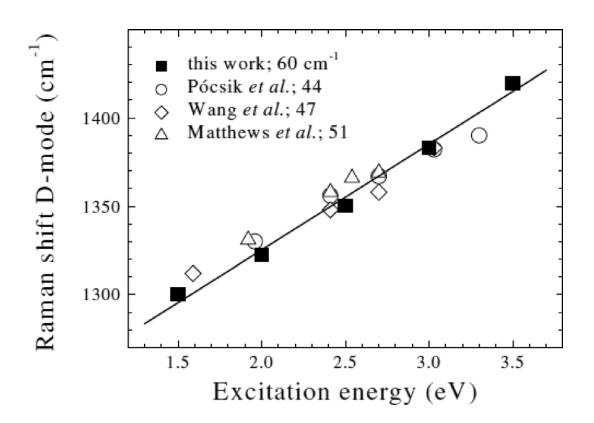


FIG. 12. Measured and calculated frequencies of the D band as a function of the excitation energy. Reproduced with permission from C. Thomsen and S. Reich, Phys. Rev. Lett. **85**(24), 5214–5217 (2000). Copyright 2000 The American Physical Society.

that  $I_G/I_{2D}$  is sensitive in the regime where there are few layers, increasing from 0.3 in the single layer to 0.8 in 6-layer graphene before saturating rapidly at higher n. The availability of an internal intensity standard makes this measurement useful for estimating the number of layers present in graphene.

Calizo *et al.* studied *n*-layer graphene (n=1 to 5) with visible and UV micro-Raman measurements. <sup>118</sup> They observed that the intensity of the 2D band diminishes when varying the excitation wavelength from visible (633 nm and 488 nm) to near UV (325 nm). It is also observed that  $I_G/I_{2D}$  differs in UV from visible Raman as the number of layers varies from 1 to 5. The 2D band energy is found to strongly depend on the laser line energy. Under near-UV excitation, this blueshift is as large as  $185 \, \text{cm}^{-1}$  when compared with the result from a longer wavelength. The 2D band energy versus laser energy is shown in Fig. 13. The observed dependence is explained based on the double-resonant or fully resonant process. <sup>118</sup>

As described in Sec. V, diamond may be integrated with electronic materials, such as GaN, via bonding of the two materials or direct growth. Diamond CVD growth typically begins with a mix of highly disordered carbon (DC) and fine-grained polycrystalline diamond whose texture and size develop with increasing diamond layer thickness. The nucleation layer may be composed of a mixture of nano-scale graphitic material and both graphitic and diamond-like amorphous carbon. 109 Stress in the diamond may be checked by the position of the sharp  $O(\Gamma)$  phonon near 1332 cm<sup>-1</sup> using the stress coefficient in Eq. (7). One indicator of diamond quality is the linewidth of the  $O(\Gamma)$  phonon, which may vary due to the inhomogeneous stress environment and the presence of disorder. The broad fluorescence observed in CVD diamond is attributed to the presence impurities and defects.<sup>21,119</sup> While the fluorescence does not typically occlude characterization of the sharp diamond  $O(\Gamma)$  peak, it generally swamps out the broad spectrum of the amorphous phases. One standard approach to obviate this competition is to carry out Raman measurements in a wavelength range where the fluorescence is weak, i.e., in the near-UV for diamond. An additional advantage of Raman measurements of

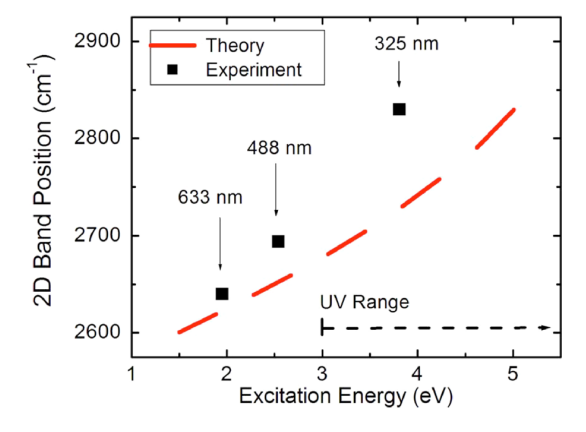


FIG. 13. Spectral position of the second-order 2D band in the Raman spectrum of graphene as a function of the laser excitation energy. Reproduced with permission from J. Appl. Phys. **106**(4), 043509 (2009). Copyright 2009 AIP Publishing LLC.

these materials using UV excitation is increased sensitivity to any diamond-like carbon which is present.<sup>18</sup>

Nazari and co-workers exploited the low diamond fluorescence intensity in the near-UV to investigate the microstructure of diamond grown on GaN for thermal management. 120 Of principal interest is the evolution of the diamond from the initial growth regime to the "bulk" of the 100–μm layer. The micro-Raman map was conducted along a line normal to the interface, as depicted in the inset SEM cross-section in Fig. 14(a). Spectra in Fig. 14(a), obtained at select distances from the GaN/D interface, exhibit a strong and narrow diamond  $O(\Gamma)$  phonon. Close to the interface, where diamond growth initiates, strong scatter is present from the disordered carbon (DC). The quality of the diamond films, also known as the Raman quality factor  $(QF_D)$ , can be evaluated based on the integrated Raman intensity of diamond and DC peaks as  $QF_D = \left[\frac{I_D}{I_D + I_{DC}}\right]$ . In this regard, the DC presence in the film can be quantified by  $1 - QF_D$  $=\left[\frac{I_{DC}}{I_D+I_{DC}}\right] \approx \left[\frac{I_{DC}}{I_D}\right]$ . This quantity is shown as a function of the distance (x) from the GaN/diamond interface in Fig. 14(b) for two line-scans at different locations across the interface. The data show that film quality is poorer at the GaN/D interface and that it improves as the film thickness increases. TEM analysis at the GaN/D interface results in a volume fraction of disordered carbon  $f_{DC}(0) = f_0 \sim 10\%$ .

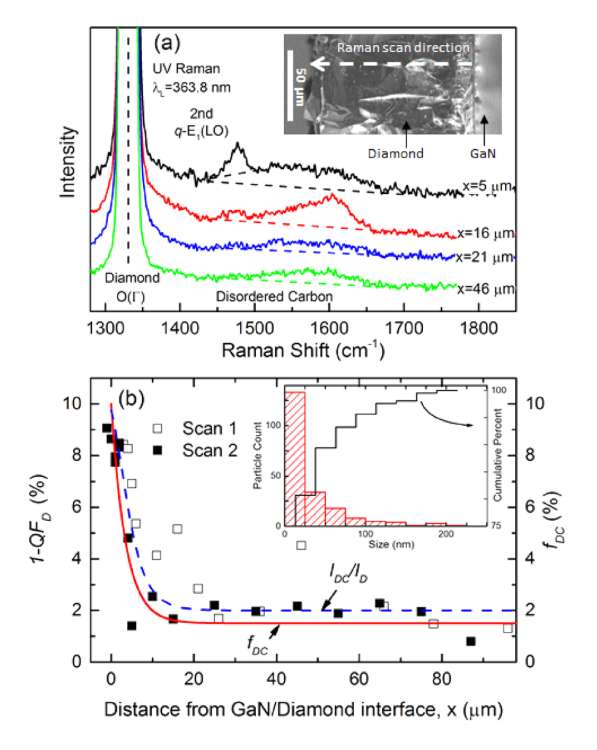


FIG. 14. (a) Micro-Raman spectra obtained with 363.8-nm excitation at different distances from the GaN/diamond interface. The inset shows the SEM cross-section, and the dashed arrow shows the direction of the line scan. (b) Non-diamond carbon fraction (left-hand axis) and associated disordered carbon (DC) volume fraction ( $f_{DC}$ , right-hand axis) versus distance from the GaN/diamond interface. Reproduced with permission from Appl. Phys. Lett. 108(3), 031901 (2016). Copyright 2016 AIP Publishing LLC.

The volume fraction of the disordered carbon is related to the quantity  $1-QF_D\approx \left[\frac{I_{DC}}{I_D}\right]$  through

$$\frac{I_{DC}}{I_D}(x) \approx A \frac{\int_0^t f_{DC}(x')\Phi(x-x')dx'}{\int_0^t \Phi(x-x')dx'},$$
(16)

where x is the central position of the laser spot along the growth direction, t is the diamond thickness, A is related to the relative Raman cross section of DC to diamond at 363.8 nm, and a simple dependence is assumed as

$$f_{DC}(x) = (f_0 - f_t)e^{-x/d} + f_t,$$
 (17)

with  $f_t$  being the DC volume fraction at larger distances from the interface and d is the characteristic length at which the DC volume fraction diminishes during CVD growth. The laser illumination  $\Phi(x)$  is discussed in Sec. II. By varying x from 0 to t and integrating over x' at each position x, function  $f_{DC}(x)$  is averaged over the laser spot size. Fitting Raman intensity data with Eq. (17), parameters A=1.3,  $f_t=1.5\%$ , and  $d=3.5~\mu{\rm m}$  are obtained. The dashed and solid curves in Fig. 14(b) show  $\frac{I_{DC}}{I_D}(x)$  and  $f_{DC}(x)$ , respectively. Without the UV measurements, obtaining the  $f_{DC}(x)$  dependence as a CVD growth diagnostic would not be possible using micro-Raman spectroscopy.

UV micro-Raman mapping has also been used to study the stress in diamond grown selectively on silicon substrates. Selective growth is attractive because it provides a route to global stress relaxation despite the presence of local stresses. This approach is developed ultimately for the integration of diamond with electronic materials. Ahmed et al. used a suspension of nanodiamond seeds in standard photoresist for obtaining a uniform spin-coat dispersal followed by patterning with standard I-line lithography. CVD diamond growth resulted in well-defined diamond structures including stripes and fields. Stress in the stripes is imaged using UV micro-Raman mapping. Rather than using a point focus and successively stepping to achieve a map, a line-focus was implemented in the micro-Raman apparatus<sup>122</sup> with the illumination traversing diamond stripes of various widths. The collected Raman scatter ultimately focused on the CCD detector to obtain information about the stress in one snapshot.

Figure 15 shows phonon shifts for the silicon substrate and diamond stripes. The shifts may be converted to stress using Eq. (7) in Sec. II. In addition to the advantage of measuring in a wavelength range where there is little fluorescence from the diamond, the UV approach also provides stress estimates in the topmost  $\sim$ 5 nm of the silicon, i.e., where the stress is expected to be the greatest. To interpret the stress, finite element (FE) simulations were carried out by incorporating the thermal stresses when the wafer is cooled from the CVD growth 720–750 °C range to ambient room temperature. The simulations shown in Fig. 15 illustrate well the stress in the diamond stripes. In silicon, the stress diminishes with distance z from the surface/interface. Therefore, the comparison of the measurement and simulation requires a depth average of the simulation data using

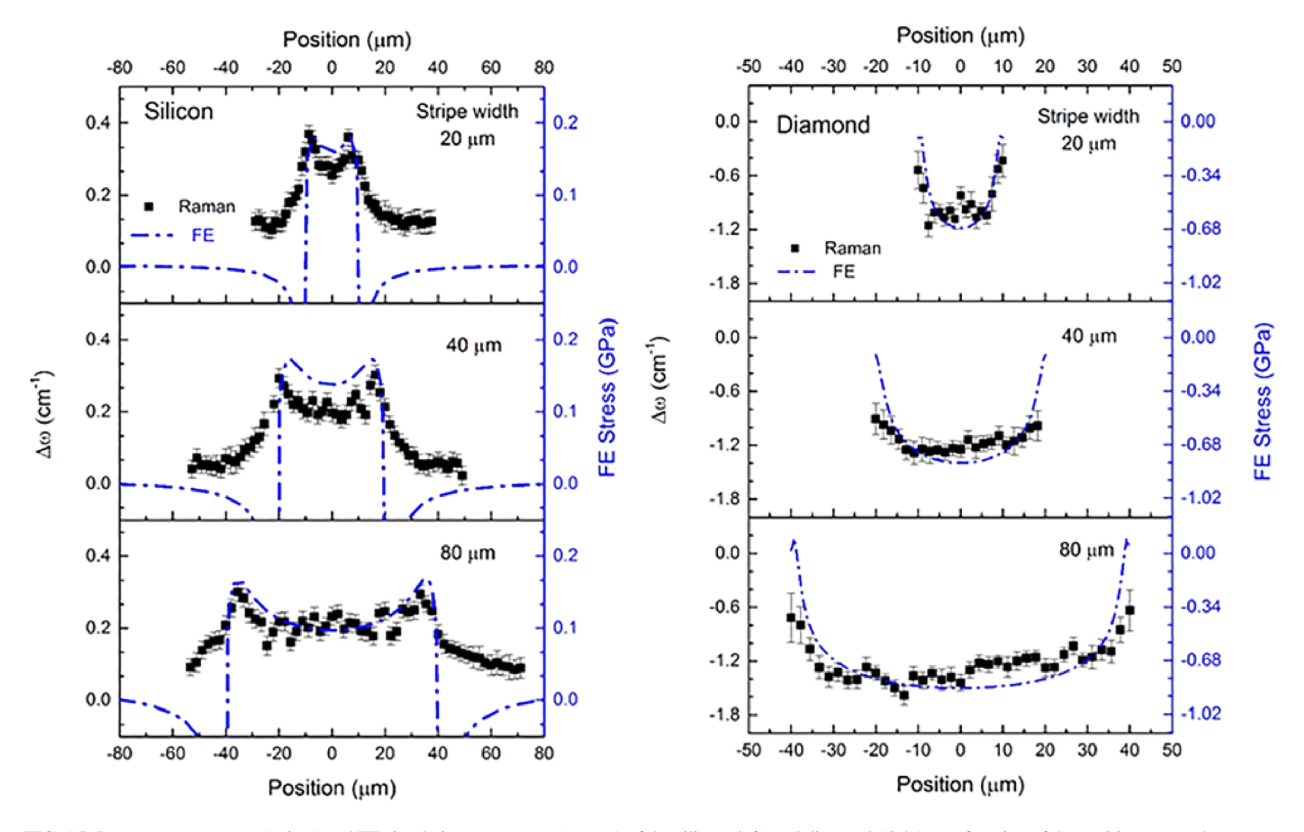


FIG. 15. Raman measurement (points) and FE simulation stress maps (curves) of the silicon (left) and diamond (right) as a function of the position across three representative stripe widths: 20, 40, and 80  $\mu$ m. Reproduced with permission from Appl. Phys. Lett. 112(18), 181907 (2018). Copyright 2018 AIP Publishing LLC.

$$\left\langle \sigma_{x'x'}(Si) \right\rangle = \frac{\int_0^\infty \sigma_{x'x'}(z) e^{-z/d_{OPT}} dz}{\int_0^\infty e^{-z/d_{OPT}} dz},$$
 (18)

where x' corresponds to a silicon (110) direction and the exponential function describes net attenuation of the incident and scattered light. This study effectively capitalizes on two key advantages to near-UV micro-Raman spectroscopy: the reduced fluorescence from CVD diamond in this wavelength range and the shallow penetration into the silicon substrate.

Ultimately, the need for better heat management through integration of electronic materials with diamond relies on improving thermal conductivity,  $\kappa$ . A necessary part of this is reliable determination of  $\kappa$  and the inevitable thermal boundary resistance (TBR) between any two materials. There has been significant progress in developing optical approaches for measuring  $\kappa^{54,123-131}$  including a design based on optical heating of a suspended graphene bridge <sup>129</sup> and electrical heating of a diamond membrane test structure. <sup>123</sup> The latter is depicted in Figs. 16(a) and 16(b). <sup>125,126</sup>

Squires et al.  $^{126}$  and Nazari et al.  $^{125}$  used near-UV micro-Raman mapping to measure lateral thermal conductivity,  $\kappa$ , in  $1-\mu$  m-thick diamond membranes grown on silicon substrates by driving a micro-fabricated heater, Fig. 16.  $\kappa$  is estimated through measuring the redshift in the phonon energy of diamond  $O(\Gamma)$  mode as a function of the distance from the heat source. This parameter is used to determine thermal conductivity using Fourier's law

$$\mathbf{q} = -\kappa \nabla T,\tag{19}$$

where q is the heat flux (e.g., in W/m²) and  $\kappa$ , which refers primarily to the in-plane thermal conductivity of the diamond, is assumed to be single-valued. The diamond thickness is an important parameter in this approach. The film thickness is precisely measured and mapped using non-destructive spectroscopic ellipsometry. <sup>125,126</sup> Knowing q produced by the current driven through the heater, and using micro-Raman mapping to establish  $\nabla T$  along the direction of the dashed line in Fig. 16(a), we may estimate  $\kappa$ .

Since both the temperature and stress shift the phonon energy, it is generally required to holistically treat these factors to arrive at a precise and reliable thermal conductivity analysis. Non-uniform thermal stress, arising from driving the heater, is not readily taken into account in the simple Fourier's law analysis. Accomplishing this combined analysis is undertaken using finite-element simulations. One way to obviate this complications due to thermal stress is by establishing a *local* temperature sensor. 132,133 Such a local temperature sensor would ideally have the following attributes: (1) provide a measure of local T, (2) not be affected by the mechanical/thermal stresses, (3) not perturb the temperature distribution in the device, and (4) readily measurable Raman spectrum with (5) a sufficiently high phonon temperature coefficient  $d\omega/dT$ . Particles transparent to the laser excitation have the further advantages of (6) permitting the measurement of the material directly beneath them while (7) experiencing minimum laser heating. The particles should

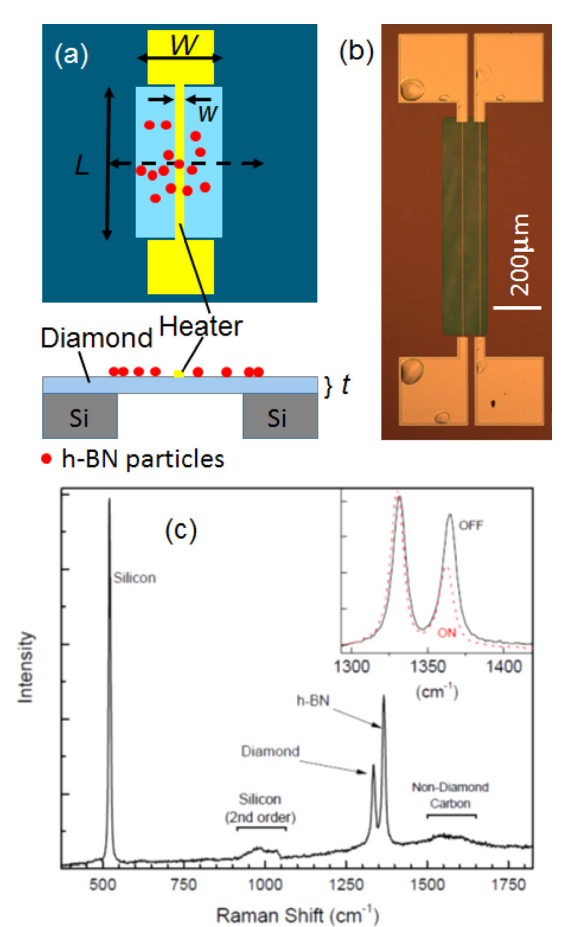


FIG. 16. (a) Plan-view and cross-section depiction of the heater structure on the diamond membrane supported by silicon and *h*-BN particle scattered on the diamond surface. (b) Photograph of the device studied. (c) Raman spectrum obtained at the position of the *h*-BN particle on diamond over silicon. The inset shows close-up spectra of diamond and *h*-BN phonons under different drive conditions. Republished with permission from Squires *et al.*, J. Phys. D: Appl. Phys. 50(24), 24LT01 (2017). Copyright 2017 IOP.

(8) require minimal or no specialized instrumentation to apply. Squires *et al.* used hexagonal boron nitride (*h*-BN) nano/micro-particles to meet all eight of these key requirements by randomly dispersing them from a liquid suspension.

The h-BN Raman phonon at  $1367\,\mathrm{cm}^{-1}$  and diamond  $O(\Gamma)$  phonon at  $1332\,\mathrm{cm}^{-1}$  are readily measured using near-UV 363.8-nm excitation. Representative spectra are shown in Fig. 16(c). The lateral physical isolation of the h-BN particles means that they will not be subject to the thermal stress in the diamond, while good thermal contact with the diamond ensures an accurate measurement of temperature based on the h-BN phonon position. The subsequent, independent measure of temperature gradient from that based on the nearby diamond phonon mode permits determination of  $\kappa$  from the simple analysis of Eq. (19) and the finite-element simulations employing data from the diamond film. Using this approach, the authors reported thermal conductivity for a  $\sim 1\,\mu\mathrm{m}$  thick CVD diamond layer to be  $76\pm8\,\mathrm{W/m}$  K and  $78.4^{+8.6}_{-5.1}$  W/m K from h-BN and diamond analysis, respectively. The value obtained from h-BN analysis is reasonably close to the value from complicated

diamond analysis. This demonstrates effectively the usefulness of the *h*-BN particles as the local sensor.

### VII. SUMMARY

Near-UV Raman and micro-Raman spectroscopy has been applied over the past *ca*. 20 years for examining the diverse properties of electronic materials. This work has aimed at taking advantage of attributes specific to the near-UV spectroscopy which are advantageous relative to the more standard visible Raman spectroscopy.

One of the specific attributes of working in the near-UV includes reduction in the laser spot size possible in micro-Raman measurements, as described in studies of silicon and silicon-related device structures.  $^{22,64,75-80}$  The improved spatial resolution is illustrated nicely in Fig. 5 from the study by Ogura  $et\ al.$  <sup>65</sup> The advantage of higher spatial resolution has recently been exploited by Ryo  $et\ al.$  to characterize silicon nanowires, as shown in Fig. 6. <sup>86</sup> Also of interest in studies of silicon and closely related alloys is the advantage of the shallow optical penetration depth of near-UV laser light. This was first leveraged by Holtz  $et\ al.$  as described above. <sup>64,91</sup> The value of  $d_{opt} \sim 5$  nm is ideal for examining the properties of ultra-shallow device layers.

The shallow  $d_{opt}$  of near-UV excitation has also been used in GaN to investigate the self-heating that takes place in AlGaN HEMT structures. In these devices, used for power electronics, the current flows in the <10-nm thick 2DEG resulting in aggressive self-heating. The  $d_{opt}$  for near-UV light in GaN makes micro-Raman measurements ideal for determining the temperature rise in the 2DEG. This has been studied by Ahmad  $et\ al.^{66,67}$  and Nazari  $et\ al.^{68}$  for HEMTs grown, respectively, on 6H-SiC and Si substrates. The latter used a micro-Raman multispectral approach to depth profile temperature rise throughout the multilayer stack, including the topmost GaN where  $\Delta T$  is the highest (Fig. 9). Alarcón-Lladó  $et\ al.$  have applied the approach to the study of self-heating in InGaN/GaN LEDs.  $^{104}$ 

The shallow  $d_{opt}$  in GaN has also been used to examine stress in the near-surface region of device layers. Particularly interesting is the full-wafer integration of an AlGaN HEMT stack with diamond for future thermal management applications.  $^{30,105}$  Cross-wafer stress mapping was found to be very consistent based on visible micro-Raman measurements, which average stress throughout the transparent GaN layer, and based on near-UV studies from each wafer side (topmost GaN and GaN/D interface). However, a stress gradient was observed in the GaN layer which was interpreted based on variations in the TD density: high in the initial GaN growth regime and lower in the region of GaN where devices are ultimately processed.

In both Si and GaN, resonance effects are important since the near-UV light excites direct electronic transitions for producing shallow optical probing. In contrast, the importance of wavelength tuning relative to the electronic structure has been applied to explain strong shifts observed in disorder-related phonons when measuring Raman spectra of graphite using different laser lines.<sup>20</sup> This understanding

had subsequent implications for interpreting similar effects in two-phonon Raman features of graphene, Fig. 13. 118

Wavelength tuning is also useful in finding ranges where fluorescence is weak. When present, fluorescence can be far stronger than Raman features needed to characterize materials. An example is CVD diamond, for which visible Raman spectra are possible when the only interest is the  $O(\Gamma)$  phonon. However, when features that are less intense or broad must be investigated, the fluorescence occludes meaningful measurements. Studies using near-UV Raman generally obviate this concern and have been used to depth profile the ubiquitous non-diamond carbon that forms during the initial stages of diamond CVD. <sup>120</sup>

# **ACKNOWLEDGMENTS**

The authors would like to thank numerous collaborators for their contributions to this research. We also acknowledge grants from funding agencies that have provided support over the years including Texas Instruments, Inc., the U.S. Army, DARPA, the National Science Foundation, and the State of Texas. Current funding for this work was provided in part by the Army Research Office (W911NF-15-1-0424), under the direction of Dr. Joe Qui, and by the National Science Foundation under Grant No. ECCS-1810419.

- <sup>1</sup>M. Cardona, *Light Scattering in Solids*, 1st ed. (Springer, Berlin, 1975).
- <sup>2</sup>M. Cardona and G. Güntherodt, *Light Scattering in Solids II* (Springer, Berlin, 1982).
- <sup>3</sup>B. Jusserand and M. Cardona, Top. Appl. Phys. **66**, 49–152 (1989).
- <sup>4</sup>G. Abstreiter, Appl. Surf. Sci. **50**(1), 73–78 (1991).
- <sup>5</sup>L. Bergman and R. J. Nemanich, J. Appl. Phys. **78**(11), 6709–6719 (1995).
- <sup>6</sup>L. Bergman and R. J. Nemanich, Annu. Rev. Mater. Sci. **26**(1), 551–579 (1996).
- <sup>7</sup>S. C. Jain, M. Willander, and H. Maes, Semicond. Sci. Technol. **11**(5), 641 (1996).
- <sup>8</sup>H. Hiroshi, J. Phys.: Condens. Matter **14**(38), R967 (2002).
- <sup>9</sup>S. Prawer and R. J. Nemanich, Philos. Trans. R. Soc., A **362**(1824), 2537–2565 (2004).
- <sup>10</sup>A. C. Ferrari, Solid State Commun. **143**(1), 47–57 (2007).
- <sup>11</sup>T. Beechem, S. Graham, S. P. Kearney, L. M. Phinney, and J. R. Serrano, Rev. Sci. Instrum. **78**(6), 061301 (2007).
- <sup>12</sup>R. Saito, M. Hofmann, G. Dresselhaus, A. Jorio, and M. S. Dresselhaus, Adv. Phys. **60**(3), 413–550 (2011).
- <sup>13</sup>A. Zoubir, *Raman Imaging* (Springer, Berlin, 2012).
- <sup>14</sup>A. Cantarero, Procedia Mater. Sci. 9, 113–122 (2015).
- <sup>15</sup>J. Wei, Z. Bing, and O. Yukihiro, J. Raman Spectrosc. 47(1), 51–58 (2016).
- <sup>16</sup>W. Sebastian, H. Joseph Razzell, and K. Ji-Seon, J. Phys. D: Appl. Phys. 50(7), 073001 (2017).
- <sup>17</sup>J. B. Renucci, R. N. Tyte, and M. Cardona, Phys. Rev. B 11(10), 3885–3895 (1975).
- <sup>18</sup>J. Wagner, C. Wild, and P. Koidl, Appl. Phys. Lett. **59**(7), 779–781 (1991).
- <sup>19</sup>D. Behr, J. Wagner, J. Schneider, H. Amano, and I. Akasaki, Appl. Phys. Lett. 68(17), 2404–2406 (1996).
- <sup>20</sup>C. Thomsen and S. Reich, Phys. Rev. Lett. **85**(24), 5214–5217 (2000).
- <sup>21</sup>S. M. Huang, Z. Sun, Y. F. Lu, and M. H. Hong, Surf. Coat. Technol. 151–152, 263–267 (2002).
- <sup>22</sup>E. Bonera, M. Fanciulli, and M. Mariani, Appl. Phys. Lett. 87(11), 111913 (2005).
- <sup>23</sup>E. Aytan, B. Debnath, F. Kargar, Y. Barlas, M. M. Lacerda, J. X. Li, R. K. Lake, J. Shi, and A. A. Balandin, Appl. Phys. Lett. 111(25), 252402 (2017).
- <sup>24</sup>S. A. Asher, C. R. Johnson, and J. Murtaugh, Rev. Sci. Instrum. **54**(12), 1657–1662 (1983).

- <sup>25</sup>V. I. Merkulov, J. S. Lannin, C. H. Munro, S. A. Asher, V. S. Veerasamy, and W. I. Milne, Phys. Rev. Lett. 78(25), 4869–4872 (1997).
- <sup>26</sup>D. Alexson, L. Bergman, R. J. Nemanich, M. Dutta, M. A. Stroscio, C. A. Parker, S. M. Bedair, N. A. El-Masry, and F. Adar, J. Appl. Phys. 89(1), 798–800 (2000).
- <sup>27</sup>R. Loudon, Adv. Phys. **13**(52), 423–482 (1964).
- <sup>28</sup>A. Pinczuk and E. Burstein, in *Light Scattering in Solids*, edited by M. Cardona (Springer, Berlin, 1975), pp. 23–78.
- <sup>29</sup>B. A. Weinstein and R. Zallen, in *Light Scattering in Solids IV: Electronics Scattering, Spin Effects, SERS, and Morphic Effects*, edited by M. Cardona and G. Güntherodt (Springer, Berlin, Heidelberg, 1984), pp. 463–527.
- <sup>30</sup>B. L. Hancock, M. Nazari, J. Anderson, E. Piner, F. Faili, S. Oh, D. Twitchen, S. Graham, and M. Holtz, Appl. Phys. Lett. 108(21), 211901 (2016).
- <sup>31</sup>E. Anastassakis, A. Cantarero, and M. Cardona, Phys. Rev. B 41(11), 7529–7535 (1990).
- <sup>32</sup>J. A. Sanjurjo, E. López-Cruz, P. Vogl, and M. Cardona, Phys. Rev. B 28(8), 4579–4584 (1983).
- <sup>33</sup>M. H. Grimsditch, E. Anastassakis, and M. Cardona, Phys. Rev. B 18(2), 901–904 (1978).
- <sup>34</sup>S. Choi, E. Heller, D. Dorsey, R. Vetury, and S. Graham, J. Appl. Phys. 113(9), 093510 (2013).
- <sup>35</sup>P. Perlin, C. Jauberthie-Carillon, J. P. Itie, A. S. Miguel, I. Grzegory, and A. Polian, Phys. Rev. B 45(1), 83–89 (1992).
- <sup>36</sup>T. Prokofyeva, M. Seon, J. Vanbuskirk, M. Holtz, S. A. Nikishin, N. N. Faleev, H. Temkin, and S. Zollner, Phys. Rev. B 63, 125313 (2001).
- <sup>37</sup>J. Liu and Y. K. Vohra, Phys. Rev. Lett. **72**(26), 4105–4108 (1994).
- <sup>38</sup>P. G. Klemens, Phys. Rev. **148**, 845–848 (1966).
- <sup>39</sup>B. K. Ridley, J. Phys.: Condens. Matter **8**(37), L511–L513 (1996).
- <sup>40</sup>J. Menéndez and M. Cardona, Phys. Rev. B **29**(4), 2051–2059 (1984).
- <sup>41</sup>G. Brocero, J. Sipma, P. Eudeline, G. Brocero, Y. Guhel, and B. Boudart, paper presented at the 21st International Conference on Microwave, Radar and Wireless Communications (MIKON), 2016. DOI:.
- <sup>42</sup>S. M. Hu, J. Appl. Phys. **50**(7), 4661–4666 (1979).
- <sup>43</sup>A. O. Ayhan and H. F. Nied, IEEE Trans. Compon. Packag. Technol. 22(4), 503–511 (1999).
- <sup>44</sup>U. Schwalke, Microelectron. Reliab. **41**(4), 483–490 (2001).
- <sup>45</sup>Y. B. Tian, L. Zhou, Z. W. Zhong, H. Sato, and J. Shimizu, Semicond. Sci. Technol. 26(10), 105002 (2011).
- <sup>46</sup>R. D. Trevisoli, J. A. Martino, E. Simoen, C. Claeys, and M. A. Pavanello, Microelectron. Reliab. 52(3), 519–524 (2012).
- <sup>47</sup>S. P. Patil and G. Waghmare, Int. J. Eng. Sci. Res. Technol. 4(4), 4 (2015).
- <sup>48</sup>D.-H. Kim, S. Park, D. Jung, E. Park, S.-W. Mhin, and C.-W. Lee, Microelectron. Eng. 154, 42–47 (2016).
- <sup>49</sup>K.-T. Wu, S.-J. Hwang, and H.-H. Lee, Sensors (Basel, Switzerland) 17(5), 1004 (2017).
- <sup>50</sup>E. Anastassakis, A. Pinczuk, E. Burstein, F. H. Pollak, and M. Cardona, Solid State Commun. 8(2), 5 (1970).
- <sup>51</sup>P. Perlin, I. Gorczyca, N. E. Christensen, I. Grzegory, H. Teisseyre, and T. Suski, Phys. Rev. B 45, 13307 (1992).
- <sup>52</sup>I. De Wolf, Semicond. Sci. Technol. **11**(2), 139 (1996).
- <sup>53</sup>M. Kuball and J. W. Pomeroy, IEEE Trans. Device Mater. Reliab. **16**(4), 667–684 (2016).
- <sup>54</sup>A. A. Balandin, Nat. Mater. **10**, 569 (2011).
- <sup>55</sup>G. Irmer, M. Wenzel, and J. Monecke, Phys. Status Solidi B **195**(1), 85–95 (1996).
- <sup>56</sup>R. Cuscó, N. Domènech-Amador, S. Novikov, C. T. Foxon, and L. Artús, Phys. Rev. B **92**(7), 075206 (2015).
- <sup>57</sup>D. Y. Song, M. Basavaraj, S. Nikishin, M. Holtz, V. Soukhoveev, A. Usikov, and V. Dmitriev, J. Appl. Phys. 100, 113504 (2006).
- <sup>58</sup> A. Link, K. Bitzer, W. Limmer, R. Sauer, C. Kirchner, V. Schwegler, M. Kamp, D. G. Ebling, and K. W. Benz, J. Appl. Phys. **86**(11), 6256–6260 (1999).
- <sup>59</sup>M. S. Liu, L. A. Bursill, S. Prawer, K. W. Nugent, Y. Z. Tong, and G. Y. Zhang, Appl. Phys. Lett. **74**(21), 3125–3127 (1999).
- <sup>60</sup>J. M. Hayes, M. Kuball, Y. Shi, and J. H. Edgar, Jpn. J. Appl. Phys., Part 2 39(7B), L710 (2000).
- <sup>61</sup>H. R. Phillip and E. A. Taft, Phys. Rev. **136**(5A), A1445–A1448 (1964)
- <sup>62</sup>D. E. Aspnes and A. A. Studna, Phys. Rev. B **27**(2), 985–1009 (1983).
- <sup>63</sup>L. Euna, in *Raman Imaging*, edited by A. Zoubir (Springer, Berlin, 2012), pp. 1–36.

- <sup>64</sup>M. Holtz, J. C. Carty, and W. M. Duncan, Appl. Phys. Lett. **74**, 2008–2010 (1999).
- <sup>65</sup>A. Ogura, D. Kosemura, M. Takei, H. Uchida, N. Hattori, M. Yoshimaru, S. Mayuzumi, and H. Wakabayashi, Mater. Sci. Eng., B 159–160, 206–211 (2009).
- <sup>66</sup>I. Ahmad, V. Kasisomayajula, M. Holtz, J. M. Berg, S. R. Kurtz, C. P. Tigges, A. A. Allerman, and A. G. Baca, Appl. Phys. Lett. 86, 173503 (2005).
- <sup>67</sup>I. Ahmad, V. Kasisomayajula, D. Y. Song, L. Tian, J. M. Berg, and M. Holtz, J. Appl. Phys. **100**, 113718 (2006).
- <sup>68</sup>M. Nazari, B. L. Hancock, E. L. Piner, and M. W. Holtz, IEEE Trans. Electron Devices 62(5), 1467–1472 (2015).
- <sup>69</sup>D. A. Tenne, A. K. Farrar, C. M. Brooks, T. Heeg, J. Schubert, H. W. Jang, C. W. Bark, C. M. Folkman, C. B. Eom, and D. G. Schlom, Appl. Phys. Lett. **97**(14), 142901 (2010).
- <sup>70</sup>T. Ghani, M. Armstrong, C. Auth, M. Bost, P. Charvat, G. Glass, T. Hoffmann, K. Johnson, C. Kenyon, J. Klaus, B. McIntyre, K. Mistry, A. Murthy, J. Sandford, M. Silberstein, S. Sivakumar, P. Smith, K. Zawadzki, S. Thompson, and M. Bohr, in *Proceedings of IEEE International Electron Devices Meeting* (2003), pp. 11.16.11-11.16.13.
- <sup>71</sup>G. Wang, A. Abedin, M. Moeen, M. Kolahdouz, J. Luo, Y. Guo, T. Chen, H. Yin, H. Zhu, J. Li, C. Zhao, and H. H. Radamson, Solid-State Electron. 103, 222–228 (2015).
- <sup>72</sup>Y. Qi, J. Peng, H.-C. Lo, J. R. Holt, M. Willemann, C. Gaire, S. Evans, P. Flanagan, H. Yu, O. Hu, and M. Kennett, ECS Trans. 75(8), 265–272 (2016).
- <sup>73</sup>P. Jianwei, L. Hsien-Ching, Z. Pei, H. Xiaoli, H. Yue, S. Yongjun, Q. Yi, V. Alina, S. Yanping, H. Wei, C. Dongil, A. Charlotte, C. Rick, L. Jae Gon, H. Owen, and S. Srikanth, Semicond. Sci. Technol. 33(8), 085012 (2018).
- 74T.-J. K. Liu and F. Ding, in Proceedings of ECS Meeting Abstracts MA2018-02 (2018), Vol. 31, p. 1026.
- <sup>75</sup>K. F. Dombrowski, I. De Wolf, and B. Dietrich, Appl. Phys. Lett. **75**(16), 2450–2451 (1999).
- <sup>76</sup>R. Liu and M. Canonico, AIP Conf. Proc. **683**(1), 738–743 (2003).
- <sup>77</sup>R. Liu and M. Canonico, Microelectron. Eng. **75**(3), 243–251 (2004).
- <sup>78</sup>V. Poborchii, T. Tada, and T. Kanayama, Appl. Phys. Lett. **91**(24), 241902 (2007).
- <sup>79</sup>O. Moutanabbir, M. Reiche, A. Hähnel, W. Erfurth, M. Motohashi, A. Tarun, N. Hayazawa, and S. Kawata, Appl. Phys. Lett. 96(23), 233105 (2010).
- <sup>80</sup>T. Tada, V. Poborchii, and T. Kanayama, J. Appl. Phys. **107**(11), 113539 (2010).
- <sup>81</sup>L. O'Reilly, K. Horan, P. J. McNally, N. S. Bennett, N. E. B. Cowern, A. Lankinen, B. J. Sealy, R. M. Gwilliam, T. C. Q. Noakes, and P. Bailey, Appl. Phys. Lett. 92(23), 233506 (2008).
- <sup>82</sup>W. S. Yoo, K. Kang, T. Ueda, T. Ishigaki, H. Nishigaki, N. Hasuike, H. Harima, and M. Yoshimoto, in Proceedings of 20th International Conference on Ion Implantation Technology (IIT) (2014), pp. 1–4.
- <sup>83</sup>S. Nakashima, T. Mitani, J. Senzaki, H. Okumura, and T. Yamamoto, J. Appl. Phys. **97**(12), 123507 (2005).
- <sup>84</sup>F. Cerdeira and M. Cardona, Phys. Rev. B **5**(4), 1440–1454 (1972).
- <sup>85</sup>M. Lee, E. Ko, and D.-H. Ko, J. Mater. Chem. C **5**(37), 9744–9752
- <sup>86</sup>Y. Ryo, H. Shuichiro, A. Shuhei, T. Motohiro, W. Takanobu, and O. Atsushi, Jpn. J. Appl. Phys., Part 1 56(6S1), 06GG10 (2017).
- <sup>87</sup>D. J. Paul, Adv. Mater. **11**(3), 191–204 (1999).
- 88U. Konig, in Proceedings of IEEE Colloquium on Advances in Semiconductor Devices (Ref. No. 1999/025) (1999), pp. 6/1–6/6.
- <sup>89</sup>Y. Min, C. Chia-Lin, M. Carroll, and J. C. Sturm, IEEE Electron Device Lett. 20(6), 301–303 (1999).
- <sup>90</sup>J. C. Bean, J. Vac. Sci. Technol., B **4**(6), 1427–1429 (1986).
- <sup>91</sup>M. Holtz, W. M. Duncan, S. Zollner, and R. Liu, J. Appl. Phys. 88, 2523 (2000).
- <sup>92</sup>C. Kisielowski, J. Krüeger, S. Ruvimov, T. Suski, J. W. Ager, E. Jones, Z. Liliental-Weber, M. Rubin, E. R. Weber, M. D. Bremser, and R. F. Davis, Phys. Rev. B 54, 17745–17753 (1996).
- <sup>93</sup>N. E. Christensen and P. Perlin, in *Gallium Nitride (GaN) I*, edited by J. I. Pankove and T. D. Moustakas (Academic, New York, 1998), Vol. 50, pp. 409–430.
- <sup>94</sup>S. C. Hsu, B. J. Pong, W. H. Li, T. E. Beechem, S. Graham, and C. Y. Liu, Appl. Phys. Lett. **91**(25), 251114 (2007).
- <sup>95</sup>T. Beechem, A. Christensen, D. S. Green, and S. Graham, J. Appl. Phys. 106(11), 114509 (2009).

- <sup>96</sup>S. Tripathy, S. J. Chua, M. S. Hao, E. K. Sia, A. Ramam, J. Zhang, W. H. Sun, and L. S. Wang, J. Appl. Phys. **91**(9), 5840–5852 (2002).
- <sup>97</sup>I. Ahmad, M. Holtz, N. Faleev, and H. Temkin, J. Appl. Phys. 95, 1692–1697 (2004).
- <sup>98</sup>M. Chu, A. D. Koehler, A. Gupta, T. Nishida, and S. E. Thompson, J. Appl. Phys. **108**(10), 104502 (2010).
- <sup>99</sup>B. S. Kang, S. Kim, J. Kim, F. Ren, K. Baik, S. J. Pearton, B. P. Gila, C. R. Abernathy, C. C. Pan, G. T. Chen, J. I. Chyi, V. Chandrasekaran, M. Sheplak, T. Nishida, and S. N. G. Chu, Appl. Phys. Lett. 83(23), 4845–4847 (2003).
- <sup>100</sup> K. D. Chabak, J. K. Gillespie, V. Miller, A. Crespo, J. Roussos, M. Trejo, D. E. Walker, G. D. Via, G. H. Jessen, J. Wasserbauer, F. Faili, D. I. Babic, D. Francis, and F. Ejeckam, IEEE Electron Device Lett. 31(2), 99–101 (2010).
- <sup>101</sup>Q. Wu, Y. Xu, J. Zhou, Y. Kong, T. Chen, Y. Wang, F. Lin, Y. Fu, Y. Jia, X. Zhao, B. Yan, and R. Xu, ECS J. Solid State Sci. Technol. 6(12), Q171–Q178 (2017).
- <sup>102</sup>C. Hodges, J. Pomeroy, and M. Kuball, J. Appl. Phys. 115(6), 064504 (2014).
- <sup>103</sup> J. Wagner, H. Obloh, M. Kunzer, M. Maier, K. Koehler, and B. Johs, J. Appl. Phys. 89, 2779–2783 (2001).
- <sup>104</sup>E. Alarcón-Lladó, S. Bin-Domanan, V. K. X. Lin, S. L. Teo, A. Dadgar, A. Krost, and S. Tripathy, J. Appl. Phys. 108(11), 114501 (2010).
- <sup>105</sup>B. L. Hancock, M. Nazari, J. Anderson, E. Piner, F. Faili, S. Oh, D. Francis, D. Twitchen, S. Graham, and M. W. Holtz, Phys. Status Solidi C 14, 1600247 (2017).
- <sup>106</sup>H. L. Duan, J. Wang, Z. P. Huang, and B. L. Karihaloo, J. Mech. Phys. Solids **53**(7), 1574–1596 (2005).
- <sup>107</sup>S. A. Solin and A. K. Ramdas, Phys. Rev. B 1(4), 1687–1698 (1970).
- <sup>108</sup>D. S. Knight and W. B. White, J. Mater. Res. 4(2), 385–393 (1989).
- <sup>109</sup>P. K. Chu and L. Li, Mater. Chem. Phys. **96**(2), 253–277 (2006).
- <sup>110</sup>A. C. Ferrari and J. Robertson, Phys. Rev. B 61(20), 14095–14107 (2000).
- <sup>111</sup>A. C. Ferrari, J. C. Meyer, V. Scardaci, C. Casiraghi, M. Lazzeri, F. Mauri, S. Piscanec, D. Jiang, K. S. Novoselov, S. Roth, and A. K. Geim, Phys. Rev. Lett. 97(18), 187401 (2006).
- <sup>112</sup>M. S. Dresselhaus, G. Dresselhaus, and P. C. Eklund, J. Raman Spectrosc. 27(3–4), 351–371 (1996).
- <sup>113</sup>M. S. Dresselhaus, G. Dresselhaus, R. Saito, and A. Jorio, Phys. Rep. 409(2), 47–99 (2005).
- <sup>114</sup>J. Maultzsch, S. Reich, and C. Thomsen, Phys. Rev. B **70**(15), 155403 (2004).
- <sup>115</sup>D. Graf, F. Molitor, K. Ensslin, C. Stampfer, A. Jungen, C. Hierold, and L. Wirtz, Nano Lett. 7(2), 238–242 (2007).
- <sup>116</sup>A. Gupta, G. Chen, P. Joshi, S. Tadigadapa, and P. C. Eklund, Nano Lett. 6(12), 2667–2673 (2006).
- <sup>117</sup>I. Calizo, A. A. Balandin, W. Bao, F. Miao, and C. N. Lau, Nano Lett. 7(9), 2645–2649 (2007).
- <sup>118</sup>I. Calizo, I. Bejnari, M. Rahman, G. Liu, and A. A. Balandin, J. Appl. Phys. **106**(4), 043509 (2009).
- <sup>119</sup>B. Marchon, G. Jing, K. Grannen, G. C. Rauch, J. W. Ager, S. R. P. Silva, and J. Robertson, IEEE Trans. Magn. 33(5), 3148–3150 (1997).
- <sup>120</sup> M. Nazari, B. L. Hancock, J. Anderson, A. Savage, E. L. Piner, S. Graham, F. Faili, S. Oh, D. Francis, D. Twitchen, and M. Holtz, Appl. Phys. Lett. 108(3), 031901 (2016).
- <sup>121</sup>R. Ahmed, M. Nazari, B. L. Hancock, J. Simpson, C. Engdahl, E. L. Piner, and M. W. Holtz, Appl. Phys. Lett. 112(18), 181907 (2018).
- <sup>122</sup>K. A. Christensen and M. D. Morris, Appl. Spectrosc. **52**(9), 1145–1147 (1998).
- <sup>123</sup>J. Anaya, S. Rossi, M. Alomari, E. Kohn, L. Tóth, B. Pécz, K. D. Hobart, T. J. Anderson, T. I. Feygelson, B. B. Pate, and M. Kuball, Acta Mater. 103, 141–152 (2016).
- A. Sood, J. Cho, K. D. Hobart, T. I. Feygelson, B. B. Pate, M. Asheghi,
   D. G. Cahill, and K. E. Goodson, J. Appl. Phys. 119(17), 175103
   (2016)
- <sup>125</sup>M. Nazari, B. Logan Hancock, J. Anderson, K. D. Hobart, T. I. Feygelson, M. J. Tadjer, B. B. Pate, T. J. Anderson, E. L. Piner, and M. W. Holtz, Solid-State Electron. 136, 6 (2017).
- <sup>126</sup>B. Squires, B. L. Hancock, M. Nazari, J. Anderson, K. D. Hobart, T. I. Feygelson, M. J. Tadjer, B. B. Pate, T. J. Anderson, E. L. Piner, and M. Holtz, J. Phys. D: Appl. Phys. 50(24), 24LT01 (2017).

- <sup>127</sup>A. Sood, R. Cheaito, T. Bai, H. Kwon, Y. Wang, C. Li, L. Yates, T. Bougher, S. Graham, M. Asheghi, M. Goorsky, and K. E. Goodson, Nano Lett. 18(6), 3466–3472 (2018).
- Lett. 16(6), 3406–3472 (2016).
   Lett. Yates, J. Anderson, X. Gu, C. Lee, T. Bai, M. Mecklenburg, T. Aoki, M. S. Goorsky, M. Kuball, E. L. Piner, and S. Graham, ACS Appl. Mater. Interfaces 10(28), 24302–24309 (2018).
   A. A. Balandin, S. Ghosh, W. Bao, I. Calizo, D. Teweldebrhan, F. Miao,
- <sup>129</sup>A. A. Balandin, S. Ghosh, W. Bao, I. Calizo, D. Teweldebrhan, F. Miac and C. N. Lau, Nano Lett. 8(3), 902–907 (2008).
- <sup>130</sup>H. Malekpour, P. Ramnani, S. Srinivasan, G. Balasubramanian, D. L. Nika, A. Mulchandani, R. K. Lake, and A. A. Balandin, Nanoscale 8(30), 14608–14616 (2016)
- <sup>131</sup>H. Malekpour and A. A. Balandin, J. Raman Spectrosc. 49(1), 106–120 (2018).
   <sup>132</sup>R. B. Simon, J. W. Pomeroy, and M. Kuball, Appl. Phys. Lett. 104(21), 213503 (2014).
- 213503 (2014).

  133 J. Anaya, S. Rossi, M. Alomari, E. Kohn, L. Toth, B. Pecz, and M. Kuball, Appl. Phys. Lett. **106**(22), 223101 (2015).